GEOLOGICA CARPATHICA, 2026, 77, 6, 493–510 https://doi.org/10.31577/GeolCarp.2026.26

Tectonometamorphic evolution of the Karakoram Metamorphic Complex, Hunza Valley, North Pakistan: Insights into microstructures and thermodynamic modelling

RAFIQUE AHMAD[1,2,✉], ASGHAR ALI[1], ONDREJ NEMEC[3] and MARIÁN PUTIŠ[3]

[1]Department of Geology, University of Peshawar, Peshawar-25130, Pakistan
[2]Department of Geology, Bacha Khan University Charsadda, Charsadda-24420, Pakistan
[3]Department of Mineralogy, Petrology and Economic Geology, Faculty of Natural Sciences, Comenius University, Bratislava, Ilkovičova 6, 842 15 Bratislava, Slovakia

(Manuscript received March 18, 2026; accepted in revised form October 26, 2026; Associate Editor: Dražen Balen)

Abstract: Detailed microstructural analysis, mineral chemistry, as well as thermodynamic modelling for P–T estimates were used to investigate the metamorphic evolution of diverse lithologies, including orthogneisses, metapelites, and migmatitic gneisses within the Karakoram Metamorphic Complex (KMC) in Hunza, North Pakistan. The findings of this study provide new insights into the tectonic evolution of the southern margin of the Eurasian Plate. Well-developed garnet porphyroblasts record progressive polyphase deformation, where continuous S_1 inclusion trails and matrix S_2 fabrics are overprinted by a late stage S_3 foliation, which record polyphase deformation histories during garnet growth. P–T estimates and pseudosection plots in MnO–Na_2O–CaO–K_2O–FeO–MgO–Al_2O_3–SiO_2–H_2O–TiO_2–O_2 (MnNCKFMASHTO) system provide peak metamorphic conditions in the region. The peak P–T conditions of ~780–820 MPa and ~640–680 °C are linked to the ongoing collision between the Indian and Eurasian plates. These data suggest that crustal thickening during continental collision was followed by several stages of deformation, which likely reflect the redistribution of strain during the late stages of orogeny, when the partially molten middle crust was uplifted and exposed by tectonic uplift and erosion.

Keywords: Karakoram Metamorphic Complex, Hunza Valley, microscopic structures, P–T pseudosections

Introduction

During the Eocene, the gigantic Himalayas were formed due to the India–Asia continental collision along the northernmost leading margin of the Indian plate, whereas the Hindu Kush, Karakoram Range, and Tibetan Plateau were formed in the Late Cretaceous along the Asian plate southern margin (e.g., Phillips et al. 2013; Borneman et al. 2015). The thermobarometric and geochronological characteristics of the Indian plate rocks have been thoroughly investigated in the past in the Nanga Parbat, Besham, and Swat regions (Le Fort et al. 1995; Searle et al. 2003; Cottle et al. 2009; Shah et al. 2011; Larson et al. 2019 and references therein; Guevara et al. 2022), as well as those of the Kohistan–Ladakh island arc between the two continental plates (Villa et al. 1996; Rolfo et al. 1997). Unlike the lithologies and tectonic units of the Indian Plate, the multiply deformed metamorphosed rocks exposed on the Eurasian plate are more dispersed. As a result, understanding the overall effects of the continent–continent collisional zones between the Indian and Eurasian/Asian plates in central Tibet and north Pakistan is considerably more challenging.

Phase equilibria modelling of metamorphic mineral assemblages including garnet has been increasingly used in combination with detailed microstructural analysis to reconstruct complex tectonic histories (Sharib & Bell 2011; Ali et al. 2016; Larson et al. 2019; Putiš et al. 2025). In particular, studies of matrix foliations and inclusion trails preserved in multiple porphyroblast generations can offer valuable insight into complex regional tectonic scenarios (e.g., Lemennicier et al. 1996; Aerden 1998; Bell et al. 1998; Ali 2010). Thermodynamic phase equilibria models can be combined with petrographic data, mineral compositions, and accessory mineral dating to effectively record the Pressure–Temperature–time–Deformation (P–T–t–D) paths of multiply deformed metamorphosed rocks within an orogenic belt (e.g., Sanislav & Bell 2011; Weller et al. 2013; Larson et al. 2019 and references therein; Putiš et al. 2025).

This paper presents amphibolite facies rocks of the southern Karakoram Metamorphic Complex (KMC) representing the Asian plate margin. They are well-exposed along the north dipping Main Karakoram Thrust (MKT) in north Pakistan (Fig. 1) and are highly suitable for constructing P–T pseudosections because they preserve mineral assemblages that closely approach chemical equilibrium during metamorphism.

We present detailed petrographic descriptions with special attention to micro–textures, combined with mineral chemistry data and the intersection of garnet end member isopleths

✉ corresponding author: Rafique Ahmad
rafique.ahmad@bkuc.edu.pk

Open Access CC BY-NC-ND

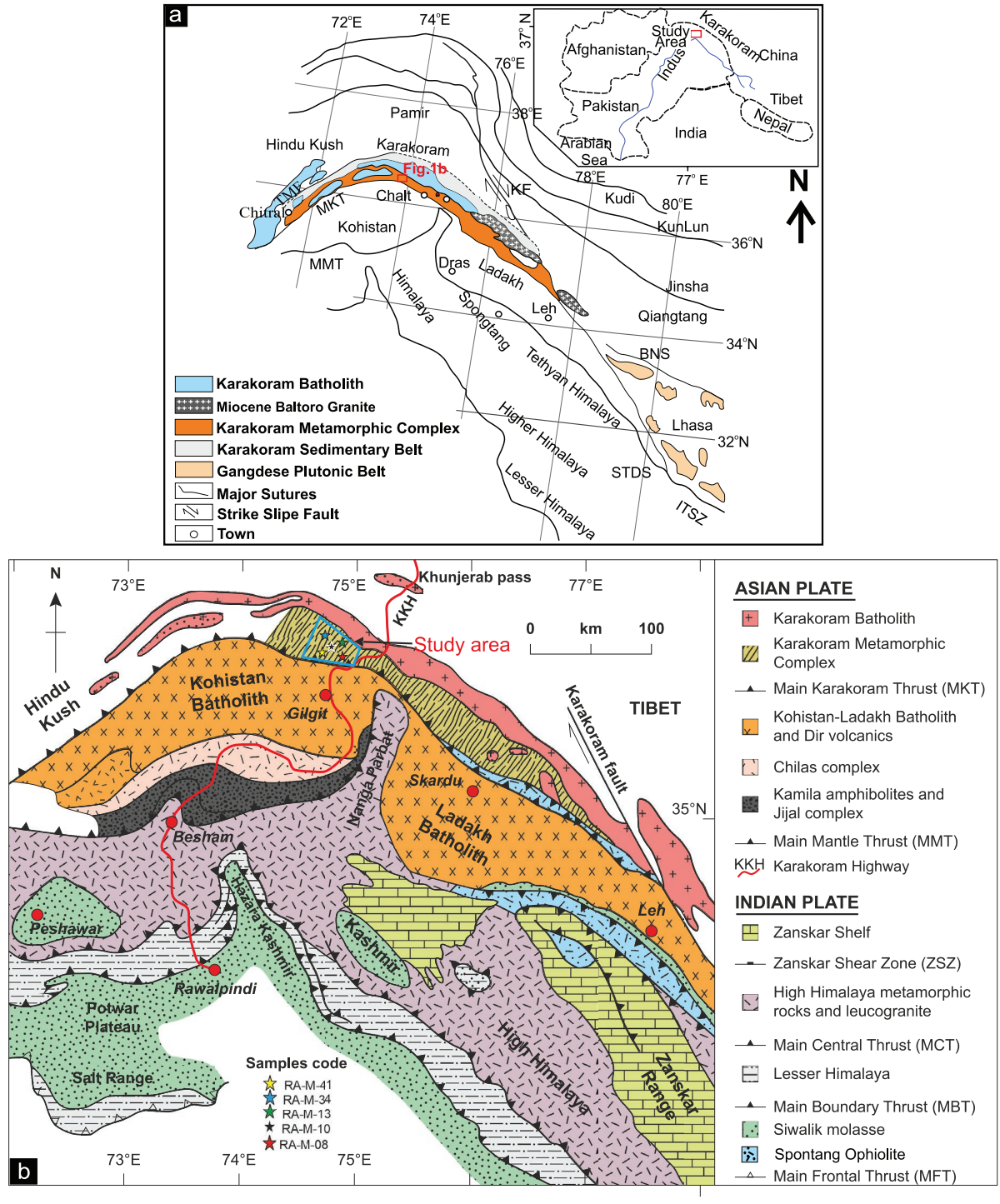


Fig. 1. (a) Regional overview of the Karakoram Block displaying significant tectonic subdivisions (after Zhu et al. 2013) and study area location. **(b)** A simplified geological map of the study area, highlighting the KMC with sample locations (after Searle et al. 1999). The GPS coordinates of the samples are as follows: 36°14'15"N 74°45'01"E (sample RA–M–08), 36°16'42"N 74°42'55"E (sample RA–M–10), 36°18'00"N 74°45'52"E (sample RA–M–13), 36°20'09"N 74°34'26"E (sample RA–M–34), 36°15'19"N 74°33'10"E (sample RA–M–41).

(Prp–Sps–Grs) on the P–T pseudosection plots constructed in the MnNCKFMASHTO chemical system. The goal is to evaluate the tectonometamorphic evolution of the multiply deformed KMC amphibolite facies rocks in Hunza, North Pakistan.

Geological setting

The Karakoram Range forms a broad arc along the northern borders of Afghanistan, Pakistan, and India, as well as the southern border of China. It is characterised by significant

crustal thickening, uplift, and deep crustal exposures associated with the tectonic evolution of the Asian continent (Brandon & Romanowicz 1986). The KMC, exposed between the Karakoram Batholith and the Shyok Suture Zone or MKT, preserves important evidence of regional deformation and metamorphism (Rolland et al. 2001, 2006; Searle et al. 2010).

The Karakoram Range is equivalent to the Lhasa Block and the Qiangtang Block lying in the north of the Ladakh Gangdese Batholith. The southern part of the Karakoram, characterised by an amphibolite-facies, high-grade regional metamorphic sequence with kyanite, sillimanite, and staurolite, as well as gneiss domes containing partial melts, is classified as a major component of the KMC (Palin et al. 2012 and references therein). Karakoram Batholith forms the major part of this terrane comprising pre-collisional quartz diorite, granodiorite, adamellite and monzodiorite with post-collisional undeformed monzogranite and leucogranites (Searle & Hacker 2019). The Paleozoic sedimentary formations lying in the northern Karakoram terrane extend into the southern Pamir. U–Pb ages of zircon and monazite from the KMC reveal significant metamorphic events that occurred both prior to and following the collision between India and Asia.

Monazites from andalusite hornfels in the Hunza Valley reveal 105.5±0.8 Ma (Fraser et al. 2001; Palin et al. 2012), while monazites obtained from sillimanite gneisses yielded 63.3±0.4, c. 52–50 and 44.0±2.0 Ma (Fraser et al. 2001). Similarly, from the recent research of Ahmad et al. (2025) in the Hunza Valley, zircons from orthogneisses and metapelitic schist yielded 103±2.6 Ma while monazite from metapelitic schist produced 47±4.3 Ma. Further southward, monazite yields an age of 16.0±1.0 Ma, which indicates a systematic decrease in monazite ages from north to south. U–Th–Pb ages of granitic rocks in the Hunza Valley range from 105.7±0.5 Ma for the pre-collisional Hunza granitoids (Fraser et al. 2001) to 52–50 Ma and ~35 Ma for the post-collisional Hunza dikes (Crawford & Searle 1993; Fraser et al. 2001). The K2 and Hushe gneisses were reported by Searle et al. (1990), whereas the younger Sumayar granite yielded an age of 9.3±0.2 Ma (Hussain et al. 2024 and references therein).

Palin et al. (2012) studied the kyanite–grade gneiss in Baltoro region, where 28.0±0.5 Ma monazite ages for these rocks with high temperatures persisted until ~22±0.3 Ma. Similarly, leucogranitic dikes intruded within the Baltoro Batholith pass through regional scale fabrics preserved in the KMC, signifying that maximum metamorphism conditions with intense ductile deformation occurred ~22 Ma. Further to the north, Fraser et al. (2001) reported the Precambrian zircons dated at 1855±11 Ma, which indicates older protoliths, while younger metamorphic monazite dates, ranging from 5.4 to 3.5 Ma, suggest more recent and deeper crustal metamorphism in the region. Similarly, Searle et al. (2010) investigated the extensive Baltoro granite batholith, which is composed predominantly of monzogranites and muscovite + biotite + garnet leucogranites. This Baltoro region granitic batholith has yielded U–Pb ages between 19.8±0.5 Ma and 13 Ma.

Peak metamorphism in southern Karakoram ended at ~37 Ma (between c. 50 and 13 Ma), and most likely by 50 Ma (between 63 and 13 Ma). Significant crustal shortening and thickening stages took place before the Baltoro granitic intrusion. However, with increasing depth, crustal metamorphism continues up to 5 to 3 Ma, as evidenced from the Dassu Gneiss dome. These findings indicate that the Karakoram microplate has undergone sustained crustal thickening and synchronous regional orogenic metamorphism resulting from the India–Asia convergence; a tectonic mechanism that likely persists up to now. This is supported by GPS data showing ongoing continent-continent convergence across the Himalayan orogenic belt (Gan et al. 2007; Zubovich et al. 2016).

Methodology and analytical conditions

Polished sections of five selected samples were studied under a transmitted polarised light microscope (Leica) at the Department of Earth Sciences, Oxford University – UK and Department of Mineralogy, Petrology and Economic Geology, Comenius University – Bratislava. Additionally, EPMA for mineral chemistry determination was conducted using a JEOL Super-probe JXA–8530F and Cameca SX–100 installed at the Earth Science Institute of the Slovak Academy of Sciences (SAS) Banská Bystrica and at the ŠGÚDŠ in Bratislava, Slovakia, respectively.

Using the JEOL Super-probe JXA–8530F at SAS, Banská Bystrica, the detection limits ranged from 0.01 to 0.05 wt.% of oxide, with a focused beam diameter of 3–5 µm, a beam current of 20 nA, and an accelerating voltage of 15 kV. Different standards were used for the analyses, including wollastonite, LiF, NaCl, Al_2O_3, apatite, fayalite, TiO_2, orthoclase, albite, forsterite, rhodonite and Cr. The analysing crystals and corresponding characteristic X-ray lines used were TAP (Kα) for Si, LPET (Kα) for F, LiF (Kα) for Cl, TAP (Kα) for Al, LPET (Kα) for Ca, LiF (Kα) for Fe, LPET (Kα) for Ti, TAP (Kα) for K, TAP (Kα) for Na, LiF (Kα) for Mg, LiF (Kα) for Mn, and LiF (Kα) for Cr.

To estimate the metamorphic stages of the amphibolite facies rocks, the software packages Perple_X–version 7.1.13 (e.g., Connolly 1990, 2005; Connolly & Petrini 2002) and GeoPS–version 3.5.6; (Xiang & Connolly 2021) were employed. These packages were employed to determine stability fields of the primary minerals and their modal contents within a P–T range of 0.5–1.2 GPa and 500 and 800 °C. The modelling was performed using an 11-component chemical system, i.e., $MnO–Na_2O–CaO–K_2O–FeO–MgO–Al_2O_3–SiO_2–H_2O–TiO_2–O_2$ (MnNCKFMASHTO). The initial components of the analysed rocks were modified to align with this 11-component system in the following ways: (a) water was set in excess; (b) the entire rock composition applied for thermodynamic modelling was converted from weight percentages of oxides to molar percentages; (c) the amount of CaO was reduced to account for the expected contribution from apatite, assuming that all phosphorus is contained within that mineral, and

(d) the ratio of Fe^{2+}/Fe^{3+} for the calculations was established based on a molar $Fe_2O_3/(Fe_2O_3+FeO)$ ratio of 0.1 (Christie et al. 1986; Berry et al. 2008; Palin et al. 2016).

The thermodynamic dataset from Holland & Powell (2011) incorporates solid solution models, including Mica(W) and Bi(W) for white mica and biotite. It also features Chl(W) for chlorite, Gt(W) for garnet, Ilm(W) for ilmenite, and melt(W) for the melt phase (White et al. 2014). Additionally, plagioclase is represented by Fsp(C1) (Holland & Powell 2003), while clinozoisite–epidote is identified as Ep (HP11) (Holland & Powell 2011), both of which were integrated into the analyses.

Pure mineral phases scrutinized include quartz, rutile, kyanite, sillimanite, iron oxides, and H_2O. The ultimate pseudosections and the contoured P–T diagrams were reconstructed using mineral assemblage data sourced from Perple_X werami, which were specified for precise P–T conditions. The garnet (Prp–Sps–Grs) chemical compositions were pivotal for isopleths generation and P–T modelling. The pressure uncertainties surrounding the boundaries of the assemblage fields are approximately ±0.1 GPa and assessed at a 2σ confidence level (cf. Powell & Holland 2008).

Results

Petrography

A total of five samples were chosen for petrographic analysis, representative of high grade amphibolite facie metamorphic rocks from the Hispar, Murtzabad, Aliabad, Hassanabad, and Baltit regions of the southern KMC at GPS coordinates (see Fig. 1 caption for samples GPS coordinates).

Sample RA–M–08 (garnet–clinopyroxene–hornblende orthogneiss)

Sample RA–M–08 is a garnet–clinopyroxene–hornblende orthogneiss which hosts well-developed garnet porphyroblasts. These hypidioblastic to idioblastic garnet porphyroblasts range in diameter up to ~3 mm and exhibit spiral shaped inclusion-trails further called S_1, although these inclusion patterns likely record a polyphase deformation history (e.g., Aerden & Ruiz-Fuentes 2020; Fig. 2a).

S_1 foliation identified in the garnet porphyroblast is deflected by the main matrix S_2 foliation. The inclusions trails within the garnet porphyroblast are truncated at the rims in S_2 main matrix foliation (Fig. 2a). In the garnet core, sigmoidal inclusion trails underlined by quartz muscovite and rare biotite are truncated by the S_2 main matrix, while the well–developed S_2 main matrix foliation is characterised by aligned biotite, muscovite, and amphiboles and deflects around garnet porphyroblasts (Fig. 2a). The fractured garnet rim contains quartz, zircon, and monazite inclusions and show variable chemical composition, while the core hosts biotite and quartz inclusions (Fig. 2a). The rock also exhibits a well-developed foliation defined by the preferential alignment of elongated biotite grains. The foliation is particularly evident around the garnet grains, where the elongated biotite flakes are preferentially aligned and locally wrap around the garnet porphyroblasts. The matrix is predominantly composed of quartz and K feldspar, forming a quartz–feldspar-rich framework within which the biotite defined foliation is developed (Fig. 2b). Matrix minerals include micas (biotite and muscovite), quartz, and plagioclase with accessory apatite, zircon, and monazite. Quartz inclusions within the garnets are flattened and define spiral geometry. Most inclusion trails are discontinuous with the matrix foliation and terminate within garnet porphyroblast (Fig. 2a). However, some inclusion trails exhibit local continuity with the S_2 foliation preserved in the surrounding matrix (Fig. 2a). Most amphibole grains are preferentially aligned parallel to the S_2 matrix foliation and are intergrown with biotite and muscovite grains (Fig. 2a). Clinopyroxene, in association with amphibole, is also common in this specimen; similarly, laths of plagioclase and K feldspar occur together with clinopyroxene (Fig. 2c, d).

Most of the amphiboles are chloritised and green to light green in colour. They are aligned with S_2 and truncated by biotite and muscovite (Fig. 2a). Clinopyroxene, in association with amphibole, is also common in this specimen and form a network with plagioclase and K feldspar laths. (Fig. 2c, d).

Sample RA–M–13 (hornblende–garnet–biotite orthogneiss)

Sample RA–M–13 is essentially composed of hornblende, garnet, quartz, biotite, plagioclase and muscovite with accessory amounts of zircon, monazite and apatite (Fig. 2e and f). This sample is characterised by highly fractured hornblende, biotite, as well as deformed quartz exhibiting undulose extinction (Fig. 2e). Hornblende and biotite preferred orientation contributes to the foliation observed in this amphibolite facies orthogneiss. The anhedral to subhedral hornblende crystals are partially replaced by quartz and muscovite (Fig. 2e) due to retrogression. The matrix contains quartz, biotite, muscovite, plagioclase, ilmenite, apatite, and opaque minerals. Similarly, up to 0.3 to 0.6 mm sized garnet grains are randomly distributed in the sample. Unlike the samples RA–M–08, RA–M–10, and RA–M–41, these garnets are devoid of internal foliation (Fig. 2f).

Sample RA–M–10 (metapelitic schist)

The sample RA–M–10 is medium to coarse-grained and is characterised by garnet porphyroblasts, biotite, and quartz as major minerals, as well as trace amounts of ilmenite, rutile, monazite, and plagioclase. Subhedral garnet porphyroblasts generally range in diameter from approximately 0.5 mm to 2 mm. They contain a sigmoidal S_1 foliation defined by inclusions of quartz, ilmenite, rutile, biotite, and muscovite. This internal foliation is truncated by the surrounding matrix S_2 foliation composed of elongate quartz grains, biotite, and muscovite (Fig. 3a, b). The relatively straight geometry of S_3,

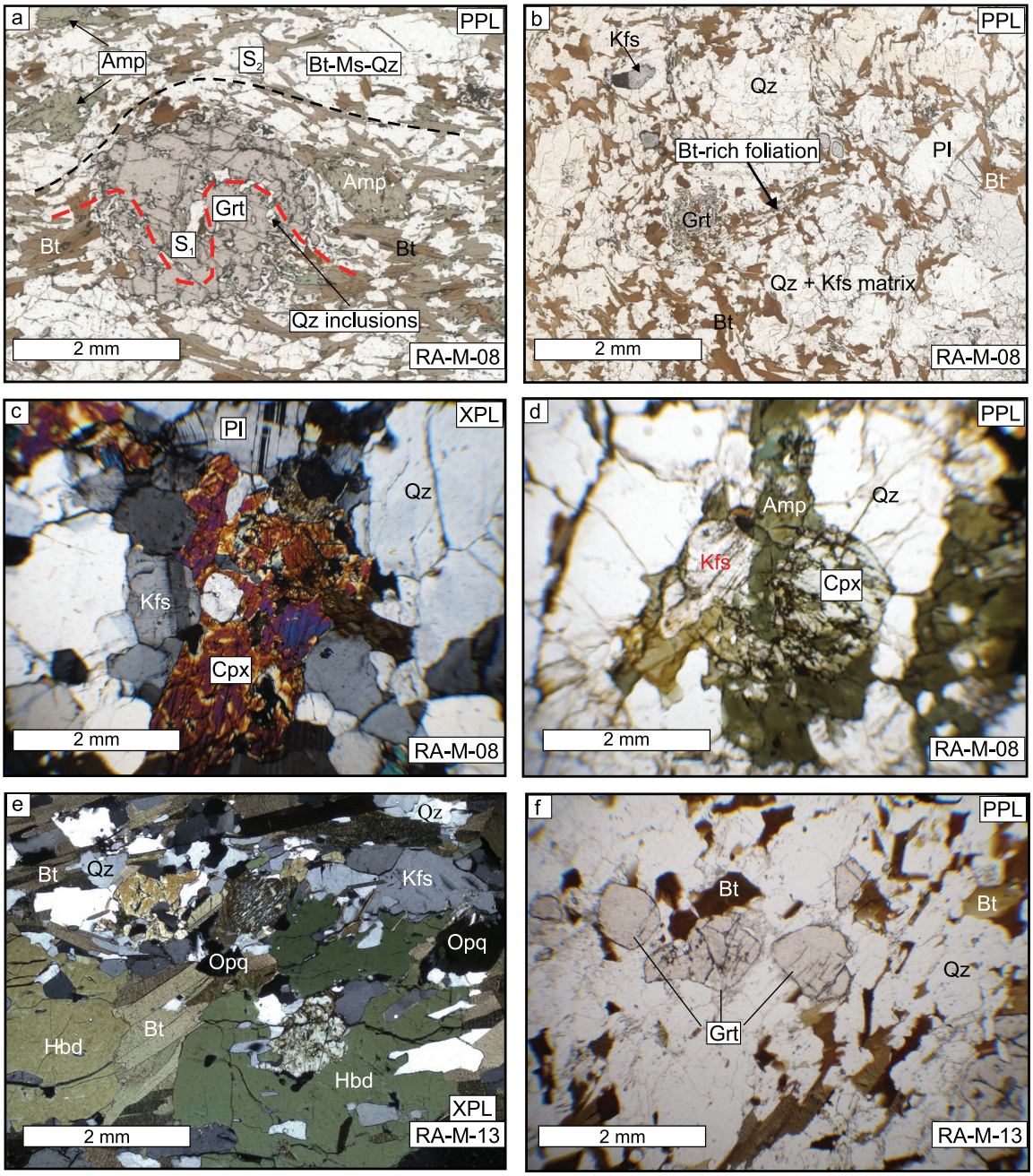


Fig. 2. (a) Photomicrographs showing different generation of garnet porphyroblast with truncated inclusion trails in the rim and core to develop S_1 and S_2 foliations. Elongated S_2 parallel biotite and muscovite intensifies around the garnet porphyroblast. Note that the biotite, muscovite, and amphibole were deflected against the garnet in the S_2 main matrix foliation. **(b)** Biotite rich foliation is truncated around garnet grains. **(c, d)** Clinopyroxene in close association with amphibole, plagioclase laths and K feldspar. This scenario exhibits the magmatic origin of rock. **(e)** Photomicrograph showing highly fractured hornblende. Breakdown of hornblende and replacement with quartz represents the retrograde metamorphism. **(f)** Well developed garnets lacking any internal structures. Note: The oriented samples are cut into P (parallel to the lineation but normal to the foliation) and N (normal to the lineation) sections following the sectioning scheme of Bell & Rubenach (1983).

compared with the curved S_1 and S_2 traces, suggests that it represents a later deformation event with a different strain geometry or shortening direction (Fig. 3b).The garnets are commonly partially replaced by biotite and muscovite within the strain shadows (Fig. 3a, b). As in the other samples, the main cleavage (S_2), defined by micas (i.e., muscovite and biotite), is intensified and deflected around the garnet porphyroblasts. The inclusion trails within the garnet are truncated at the rims by S_2. Additionally, some garnet porphyroblasts exhibit change in the asymmetry of their inclusion trails from core to rim (Fig. 3a), which therefore suggests a polyphase deformation history (e.g., Sapkota & Sanislav 2013).

Sample RA–M–34 (migmatitic gneiss)

Sample RA–M–34 is characterised by well-developed amphiboles with muscovite, quartz, K feldspar, and plagioclase. Ilmenite, zircon, monazite, and apatite are present in trace amounts in the matrix. Widely spaced foliations are defined by biotite and muscovite (Fig. 3c and d). Amphiboles of different generations are present with highly irregular margins (Fig. 3c). Garnet occurs as inclusion free porphyroblasts located within the leucosome aligned with biotite foliation. The well-developed melanosome domain with an elongated biotite and muscovite domain with leucosome K feldspar clearly suggest a granitic protolith (Fig. 3d).

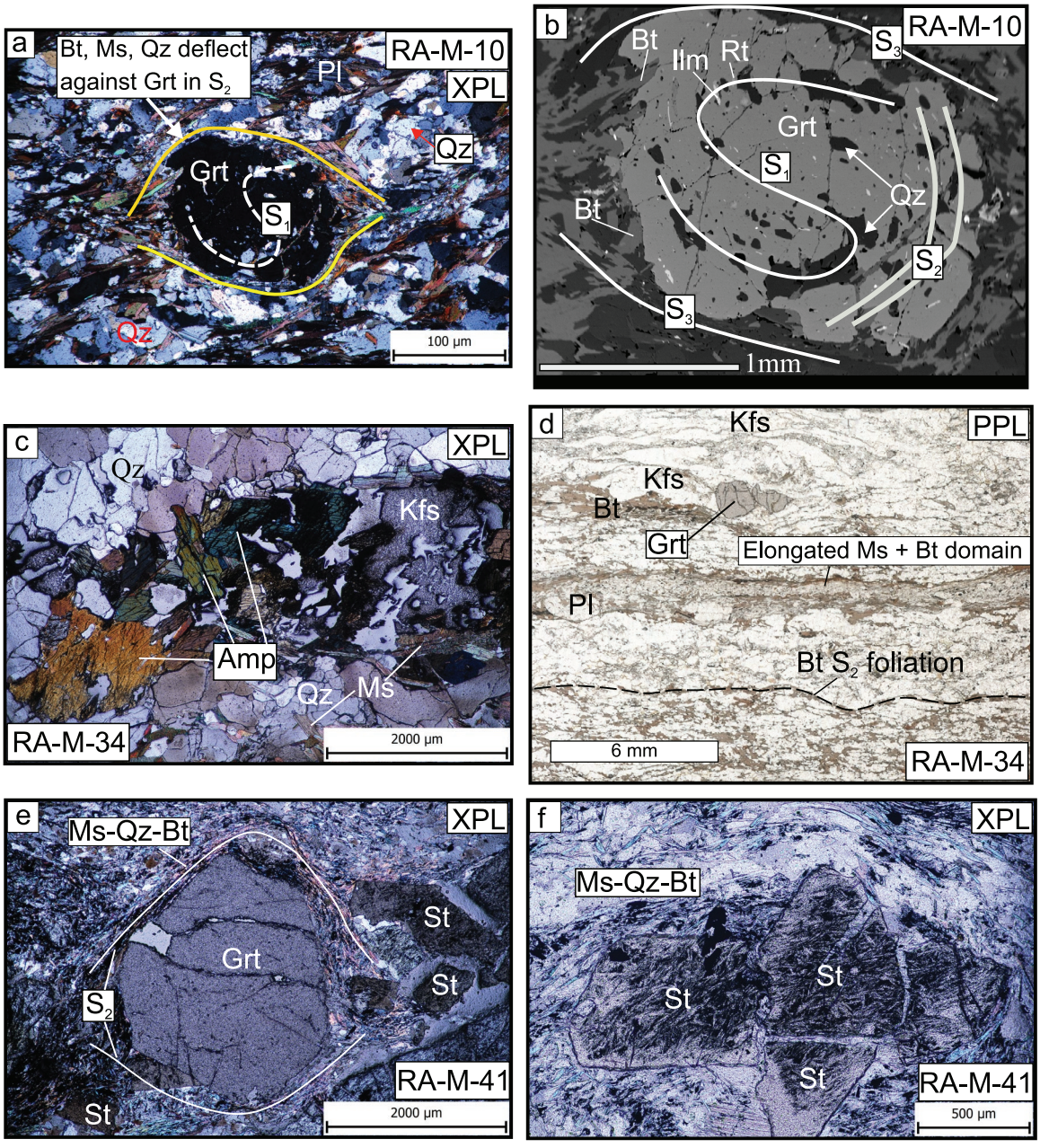


Fig. 3. (a) Photomicrograph showing the truncation of internal inclusions (S_1) and external minerals (S_2) within and around the garnet porphyroblast. **(b)** BSE image for confirmation of different trace minerals and structural behaviour of garnet to elucidate the S_1, S_2 and S_3 foliations scenario in sample RA–M–10. **(c, d)** Granitic gneiss with well-developed amphibole minerals. Biotite and muscovite are arranged in melanosome and K feldspar in leucosome. **(e)** Photomicrograph showing a garnet porphyroblast with quartz inclusions. Micas, including biotite and muscovite, and quartz are truncated in the S_2 main matrix foliation. This foliation also has some impact on staurolite minerals for orientation along with micas and quartz. **(f)** Elongated micaceous minerals bent around the highly fractured staurolite porphyroblasts. Note: The oriented samples are cut into P (parallel to the lineation but normal to the foliation) and N (normal to the lineation) sections following the sectioning scheme of Bell & Rubenach (1983).

Sample RA–M–41 (garnet–staurolite metapelitic schist)

Sample RA–M–41 is characterised by garnet and staurolite porphyroblasts with biotite, muscovite, and quartz (Fig. 3e and f). Garnet porphyroblasts (up to ~1 mm in size) are hypidioblastic to idioblastic and contain abundant inclusions of matrix phases, including quartz and graphite that tract the external pervasive and crenulation fabric (Fig. 3e). Overall, the studied rock is texturally medium to coarse-grained with quartz, ilmenite, and opaque minerals in the groundmass. Poorly defined pressure shadow zones consist of granoblastic quartz and muscovite and are found adjacent to a few garnet porphyroblasts (Fig. 3e).

This rock also exhibits a well-developed, differentiated crenulation cleavage that defines the cleavage domain and is composed predominantly of aligned muscovite, biotite, and elongated quartz ribbons. The quartz-rich domains contain abundant, well-developed staurolite porphyroblasts (~ 0.5 to 1 mm) that are pervasively fractured and locally altered. The S_2 crenulation cleavage is deflected around the staurolite porphyroblasts, with the aligned muscovite and biotite defining a continuous foliation that wraps around their margins (Fig. 3f). This microstructural relationship demonstrates that the staurolite porphyroblasts predate the development of S_2 fabric and behaved as mechanically competent phases during progressive deformation (cf. Passchier & Trouw 2005; Fig. 3f).

Mineral chemistry

Garnet

A total of five garnet porphyroblasts were analysed from sample RA–M–10 and two garnet porphyroblasts from RA–M–41 in order to study the rim, core, and mantle compositions (Tables 1 and 2).

Sample RA–M–10

In specimen RA–M–10, the molar percentage (mol.%) of almandine (X_{alm}) ranges from 69–71 mol.%, 65–70 mol.%, 65–70 mol.%, 70 mol.% and 67–70 mol.% in garnet grains Grt–1, Grt–2, Grt–3, Grt–4 and Grt–5, respectively (Table 1). The mol.% of pyrope (X_{prp}) ranges from 1–15 mol.%, 11–90 mol.%, 10–14 mol.%, 10–11 mol.% and 12–16 mol.% in garnet grains Grt–1, Grt–2, Grt–3, Grt–4 and Grt–5, respectively. The mol.% of spessartine (X_{sps}) ranges from 10–90 mol.%, 10–19 mol.%, 11–19 mol.%, 11 mol.% and 11–13 mol.% in garnet grains Grt–1, Grt–2, Grt–3, Grt–4 and Grt–5, respectively. Similarly, the mol.% of grossular (X_{grs}) ranges from 3–5 mol.%, 3–5 mol.%, 2–6 mol.%, 8 mol.% and 4–5 mol.% in garnet grains Grt–1, Grt–2, Grt–3, Grt–4 and Grt–5, respectively (Table 1).

Garnet grains analysed from sample RA–M–10 exhibit typical prograde zoning, showing a decrease in X_{sps} towards the rim (Woodsworth 1977). However, Grt–2 shows reversed zoning in the rim compared to higher X_{alm} (2.039 wt.%) and lower X_{sps} (0.52 wt.%) in their cores. Chemical profile (Fig. 4) and Table 1 confirm a general trend of X_{grs} and X_{sps} rich cores slowly changing to X_{alm} and X_{prp} rich rims. Similarly, there is a consistent trend in the profile at the outer mantle and inner rim of the studied garnet grains where X_{prp} and X_{sps} change abruptly (Fig. 4b). Furthermore, the mol.% of almandine (X_{alm}) and pyrope (X_{prp}) increases from core to rim (68–70 mol.% for almandine and 9–15 mol.% for pyrope), whereas the mol.% of spessartine (X_{sps}) and grossular (X_{grs}) decreases from core to rim (17–10 mol.% for spessartine and 6–5 mol.% for grossular; Fig. 4a, b).

Sample RA–M–41

In sample RA–M–41, the garnet composition exhibits a systematic core-to-rim variation. The mol.% of almandine (X_{alm}) increases from 81 mol.% in the core to 84 mol.% at the rim, while pyrope (X_{prp}) increases slightly from 10 to 11 mol.%. In contrast, spessartine (X_{sps}) decreases from 3 mol.% in the core to 1 mol.% at the rim, and grossular (X_{grs}) decreases from 9 to 5 mol.%. Overall, these trends indicate relative enrichment in the almandine and pyrope components towards the rim, accompanied by depletion in the spessartine and grossular components (Table 2).

In the current study, the garnet profiles are plotted for three samples, i.e., RA–M–10, RA–M–13 and RA–M–08 (Fig. 4a–f), although here, the sample RA–M–10 and sample RA–M–41 are used for P–T paths.

Biotite (sample RA–M–10)

Biotite grains have been analysed both as inclusions within the garnet and also in the strain shadow of garnet porphyroblast. Biotite has Mg ranging 2.14–2.22 atoms p.f.u. and Fe varies from 2.12 to 2.47 atoms p.f.u. (Table 3). Ti content in the studied biotites ranges from 0.15 to 0.25 atoms p.f.u while Al_{vi} shows variation from 0.75 to 0.85 atoms p.f.u. Mn is in a negligible amount (0.03 to 0.04 atoms p.f.u.), while K varies from 1.81 to 1.87 atoms p.f.u. Overall, biotite is classified as annite and phlogopite (Fig. 5) with Mg# [=(Mg/Mg+Fe)] in the range of 0.47–0.50, with a cluster between 0.47 and 0.48 (Table 3).

White mica (sample RA–M–10)

Muscovite grains have been analysed within the garnet strain shadow and in the matrix foliation. Al_{vi} content varies from 3.58 to 3.74 atoms p.f.u (Table 4). The octahedral layer of mica is predominantly filled by K and Na with ranges from 1.81 to 1.84 and 0.13 to 0.15 atoms p.f.u. respectively. The Mg/Mg+Fe ratio of muscovite ranges from 0.50 to 0.57 (Table 4; Fig. 5).

Plagioclase (sample RA–M–10)

Plagioclase laths were predominantly analysed in the matrix foliation lying close to garnet porphyroblasts. These plagioclase

Table 1: EPMA garnet mineral chemistry for sample RA–M–10.

Mineral/ An. No.	**Gt1/1**	**Gt1/2**	**Gt1/3**	**Gt1/4**	**Gt1/7**	**Gt2/12**	**Gt2/15**	**Gt2/17**	**Gt2/18**	**Gt3/22**	**Gt3/25**	**Gt3/26**	**Gt3/29**	**Gt3/33**	**Gt3/34**	**Gt3/35**	**Gt3/36**	**Gt3/37**	**Gt3/38**	**Gt3/39**	**Gt3/40**	**Gt4/42**	**Gt5/43**	**Gt5/44**	**Gt5/47**	**Gt5/48**
SiO_2 (wt.%)	36.43	37.59	36.87	36.28	36.67	35.72	35.23	36.94	36.92	36.67	35.54	36.28	36.3	37.54	37.4	37.77	37.9	37.6	38.03	37.52	37.28	37.2	36.9	36.64	36.6	36.05
TiO_2	0.01	0.01	0.01	0.01	0.02	0.03	0.01	0.04	0	0	0.03	0.01	0.02	0.03	0.04	0.07	0.02	0	0.01	0.01	0	0	0.01	0.02	0.02	0.02
Al_2O_3	21.32	21.6	21.42	20.98	21.15	21.15	20.88	21.17	21.57	21.47	20.88	21.3	21.18	21.63	21.59	21.56	21.52	21.72	21.6	21.77	22.09	21.71	21.78	21.54	21.72	21.66
FeO	32.47	32.17	32.31	31.83	32.79	31.75	30.62	30.47	32.49	32.17	31.93	32.13	31.97	30.01	30	30.37	31.08	31.8	32.26	31.84	31.8	31.93	31.45	32.21	32.72	32.22
MnO	4.25	4.28	4.32	6.47	4.8	6.1	7.96	7.63	4.45	4.91	5.11	5.65	5	8.25	8.18	7.37	6.48	5.85	5.09	4.75	6.28	5.01	4.86	5.35	4.74	5.49
MgO	3.76	3.66	3.75	2.4	2.96	2.69	2.19	2.23	3.49	3.33	3.45	2.8	3.33	2.6	2.58	2.58	2.87	3.07	3.39	3.52	2.81	2.69	3.93	3.29	3.19	2.98
CaO	1.93	1.89	1.92	1.9	1.98	1.91	1.97	2.01	1.96	2	1.99	1.92	1.99	2.18	2.26	2.15	2.04	2.05	1.95	1.97	1.97	2.73	2.13	1.98	1.96	1.9
Na_2O	0	0	0.03	0.01	0	0.05	0	0.02	0.02	0.02	0.03	0	0.04	0.01	0.03	0.01	0.03	0.02	0.02	0.02	0.02	0	0	0.02	0.01	0.02
K_2O	0	0	0	0.05	0.01	0.02	0	0.03	0	0.01	0	0.02	0.01	0.01	0.01	0	0	0	0	0	0	0	0.02	0.01	0.02	0.04
Total	**100.18**	**101.2**	**100.63**	**99.92**	**100.39**	**99.42**	**98.88**	**100.55**	**100.9**	**100.58**	**98.96**	**100.1**	**99.83**	**102.27**	**102.09**	**101.88**	**101.94**	**102.12**	**102.36**	**101.41**	**102.24**	**101.28**	**101.07**	**101.06**	**100.98**	**100.38**
Oxygen p.f.u.	**12**	**12**	**12**	**12**	**12**	**12**	**12**	**12**	**12**	**12**	**12**	**12**	**12**	**12**	**12**	**12**	**12**	**12**	**12**	**12**	**12**	**12**	**12**	**12**	**12**	**12**
Si *(a.p.f.u)*	2.929	2.979	2.947	2.95	2.953	2.918	2.907	2.978	2.947	2.941	2.906	2.937	2.936	2.969	2.964	2.989	2.995	2.968	2.987	2.97	2.946	2.962	2.932	2.93	2.929	2.91
Aliv	0.071	0.021	0.053	0.05	0.047	0.082	0.093	0.022	0.053	0.059	0.094	0.063	0.064	0.031	0.036	0.011	0.005	0.032	0.013	0.03	0.054	0.038	0.068	0.07	0.071	0.09
Alvi	1.953	1.997	1.968	1.964	1.964	1.958	1.942	1.99	1.978	1.973	1.924	1.971	1.958	1.986	1.983	2.001	2	1.991	1.988	2.002	2.003	2.001	1.974	1.962	1.979	1.973
Fe^{3+}	0.042	0.002	0.028	0.032	0.031	0.036	0.051	0.006	0.02	0.024	0.066	0.026	0.036	0.011	0.013	0	0	0.008	0.01	0	0	0	0.023	0.032	0.018	0.023
Fe^{2+}	2.142	2.13	2.132	2.133	2.179	2.134	2.062	2.048	2.149	2.133	2.118	2.149	2.126	1.974	1.975	2.017	2.055	2.092	2.109	2.111	2.106	2.127	2.067	2.121	2.172	2.152
Mn	0.29	0.287	0.292	0.445	0.328	0.422	0.556	0.521	0.301	0.334	0.354	0.387	0.342	0.553	0.549	0.494	0.434	0.391	0.339	0.318	0.42	0.338	0.327	0.362	0.321	0.376
Mg	0.451	0.432	0.446	0.29	0.355	0.328	0.27	0.268	0.415	0.399	0.42	0.337	0.402	0.306	0.304	0.304	0.339	0.362	0.397	0.416	0.331	0.32	0.466	0.392	0.38	0.359
Ca	0.166	0.161	0.164	0.165	0.171	0.167	0.174	0.174	0.168	0.171	0.175	0.167	0.173	0.185	0.192	0.182	0.173	0.174	0.164	0.167	0.167	0.233	0.181	0.169	0.168	0.165
Cations Sum	**8**	**8**	**8**	**8**	**8**	**8**	**8**	**8**	**8**	**8**	**8**	**8**	**8**	**8**	**8**	**8**	**8**	**8**	**8**	**8**	**8**	**8**	**8**	**8**	**8**	**8**
Almandine	0.69	0.7	0.69	0.69	0.71	0.68	0.65	0.67	0.7	0.69	0.67	0.69	0.69	0.65	0.65	0.67	0.68	0.69	0.7	0.69	0.69	0.7	0.67	0.68	0.7	0.7
Andradite	0.02	0	0.01	0.01	0.01	0.02	0.03	0.03	0.01	0.01	0.03	0.01	0.02	0.05	0.07	0	0	0.04	0.05	0	0	0	0.01	0.02	0	0.01
Grossular	0.03	0.05	0.04	0.04	0.04	0.04	0.03	0.05	0.05	0.04	0.02	0.04	0.04	0.06	0.06	0.06	0.06	0.05	0.05	0.06	0.06	0.08	0.05	0.04	0.05	0.04
Pyrope	0.15	0.14	0.15	0.01	0.12	0.11	0.9	0.9	0.14	0.13	0.14	0.11	0.14	0.1	0.1	0.1	0.11	0.12	0.13	0.14	0.11	0.11	0.16	0.13	0.13	0.12
Spessartine	0.1	0.9	0.1	0.15	0.11	0.14	0.19	0.17	0.1	0.11	0.12	0.13	0.11	0.19	0.18	0.16	0.14	0.13	0.11	0.11	0.14	0.11	0.11	0.12	0.11	0.13
Mg/ (Mg+Fe)	0.17	0.17	0.17	0.12	0.14	0.13	0.11	0.11	0.16	0.16	0.16	0.14	0.16	0.13	0.13	0.13	0.14	0.15	0.16	0.17	0.13	0.13	0.19	0.15	0.15	0.14

Table 2: EPMA garnet mineral chemistry for sample RA–M–41.

Mineral/An	Grt1/rim	Grt1/rim	Grt1/ mantle	Grt1/ mantle	Grt1/ core	Grt1/ core	Grt2/rim	Grt2/rim	Grt2/ mantle	Grt2/ mantle	Grt2/ core	Grt2/ core
SiO_2 (wt.%)	37.78	36.99	37.78	36.51	36.67	36.36	38.03	37.36	36.74	36.98	37.33	36.50
TiO_2	0.14	0.12	0.03	0.06	0.07	0.03	0.48	0.06	0.04	0.06	0.04	0.05
Al_2O_3	25.42	20.77	20.89	21.28	21.69	21.28	26.03	21.27	21.13	21.26	21.02	21.24
FeO	30.01	37.74	36.82	35.91	35.41	35.39	25.48	37.83	37.76	36.96	35.68	35.68
MnO	0.16	0.39	0.89	1.00	1.14	1.04	0.14	0.42	0.56	0.90	1.00	1.05
MgO	2.02	2.62	2.42	2.26	2.28	2.22	1.73	2.58	2.63	2.43	2.28	2.34
CaO	1.15	1.78	2.16	3.15	3.49	3.42	1.00	1.81	1.85	2.25	2.80	3.09
Na_2O	0.53	0.00	0.00	0.00	0.00	0.00	1.12	0.00	0.00	0.00	0.00	0.02
Total	**97.21**	**100.42**	**100.99**	**100.17**	**100.74**	**99.75**	**94.00**	**101.34**	**100.71**	**100.84**	**100.15**	**99.97**
Oxygen p.f.u.	**12**	**12**	**12**	**12**	**12**	**12**	**12**	**12**	**12**	**12**	**12**	**12**
Si *(a.p.f.u)*	3.159	2.981	2.951	2.965	3.010	2.945	3.074	2.981	3.026	2.943	2.934	2.941
Al iv	0.000	0.019	0.049	0.035	0.000	0.055	0.000	0.019	0.000	0.057	0.066	0.059
Al vi	2.548	1.982	1.952	1.974	1.998	1.966	2.437	1.955	1.972	1.965	1.980	1.970
Fe^{3+}	−0.578	0.014	0.046	0.022	0.000	0.031	−0.446	0.038	0.026	0.031	0.016	0.028
Fe^{2+}	2.347	2.509	2.489	2.455	2.406	2.376	2.486	2.504	2.439	2.388	2.352	2.364
Mn	0.010	0.029	0.038	0.061	0.068	0.072	0.011	0.027	0.060	0.068	0.077	0.071
Mg	0.214	0.307	0.315	0.290	0.274	0.282	0.245	0.315	0.289	0.272	0.271	0.268
Ca	0.089	0.155	0.159	0.193	0.242	0.267	0.100	0.154	0.185	0.272	0.300	0.297
Cations Sum	**8**	**8**	**8**	**8**	**8**	**8**	**8**	**8**	**8**	**8**	**8**	**8**
Almandine	0.88	0.83	0.82	0.81	0.80	0.79	0.87	0.83	0.82	0.79	0.78	0.78
Andradite	0.00	0.00	0.00	0.00	0.00	0	0	0.00	0.00	0.00	0.00	0.00
Grossular	0.03	0.05	0.05	0.06	0.08	0.08	0.03	0.05	0.06	0.09	0.09	0.09
Pyrope	0.08	0.10	0.10	0.09	0.09	0.09	0.08	0.10	0.09	0.09	0.09	0.89
Spessartine	0.03	0.09	0.01	0.02	0.02	0.02	0.04	0.09	0.02	0.02	0.57	0.02
Mg/(Mg+Fe)	0.08	0.11	0.11	0.10	0.10	0.10	0.10	0.11	0.11	0.10	0.10	0.10

lies in the oligoclase range varying from from 0.72 to 0.73 mole percentage regardless of their position in the matrix or near the garnet (Table 5). Furthermore, no systematic compositional variation was reported within the grains.

Amphibole (sample RA–M–08)

Following the Hawthorne et al. (2012) classification, the studied amphiboles in sample RA–M–08 correspond to magnesio-hornblende (Mg–Hbl; Fig. 6a). In the studied sample, i.e., RA–M–08 (Grt–Cpx–Hbl orthogeniss) the CaO content varies from 11.50 to 11.91 wt.%, while the SiO_2 reached as high as up to 44.87 wt.%. Similarly, the Al_2O_3 content varies between 10.80 and 11.82 wt.% and the MgO varies between 8.85 to 9.62 wt.%. The FeO content in calcium amphiboles comparatively ranges from 16.07 to 16.74 wt.%. Finally, TiO_2 and MnO in Mg–Hbl approaches 0.93 and 0.47 wt.%, respectively (Table 6; Fig. 6a).

Clinopyroxene (sample RA–M–08)

According to the classification of Morimoto et al. (1988), all the analysed clinopyroxene in sample RA–M–08 is a diopside with a composition of $En_{35–36}Fs_{15}Wo_{48–49}$. The composition of pyroxenes in the sample is quite homogenous with no visible zoning. The SiO_2 content is between 52.62 to 53.27 wt.% and CaO between 22.99 to 23.28 wt.%. Iron and magnesium content reaches up to 11.49–12.85 wt.% of FeO and 9.98–10.44 MgO, respectively. Concentration of Na_2O is mostly negligible up to 0.29 wt.% together with MnO up to 0.57wt.%. NiO up to 0.04 wt.% and Cr_2O_3 (up to 0.05 wt.%) are below the detection limit (Table 7; Fig. 6b).

P–T conditions

P–T pseudosections illustrate a pattern of multi-variant reactions involving metamorphic index minerals within the P–T space (White et al. 2007). Several reconnaissance calculations were performed on samples RA–M–10 (metapelitic schist) and RA–M–41 (garnet–staurolite metapelitic schist) in order to reconstruct the evolution of the observed mineral assemblages. The selected P–T pseudosections (Figs. 7, 8) were contoured with isopleths for the garnet molar fractions (Xprp, Xsps, Xgrs). The reconstructed P–T estimates are established on the compositional characteristics and modal content of garnet, as well as on the stability fields of other mineral assemblages. Overlapping or at least a proximity of the corresponding isopleths leads to P–T conditions for the garnet core, allowing reconstruction of the metamorphic path and determination of peak pressure and temperature values. For the modelling, the bulk rock analyses of samples RA–M–10 and RA–M–41 (Table 8) were used and modified based on the approach described in the methodology section.

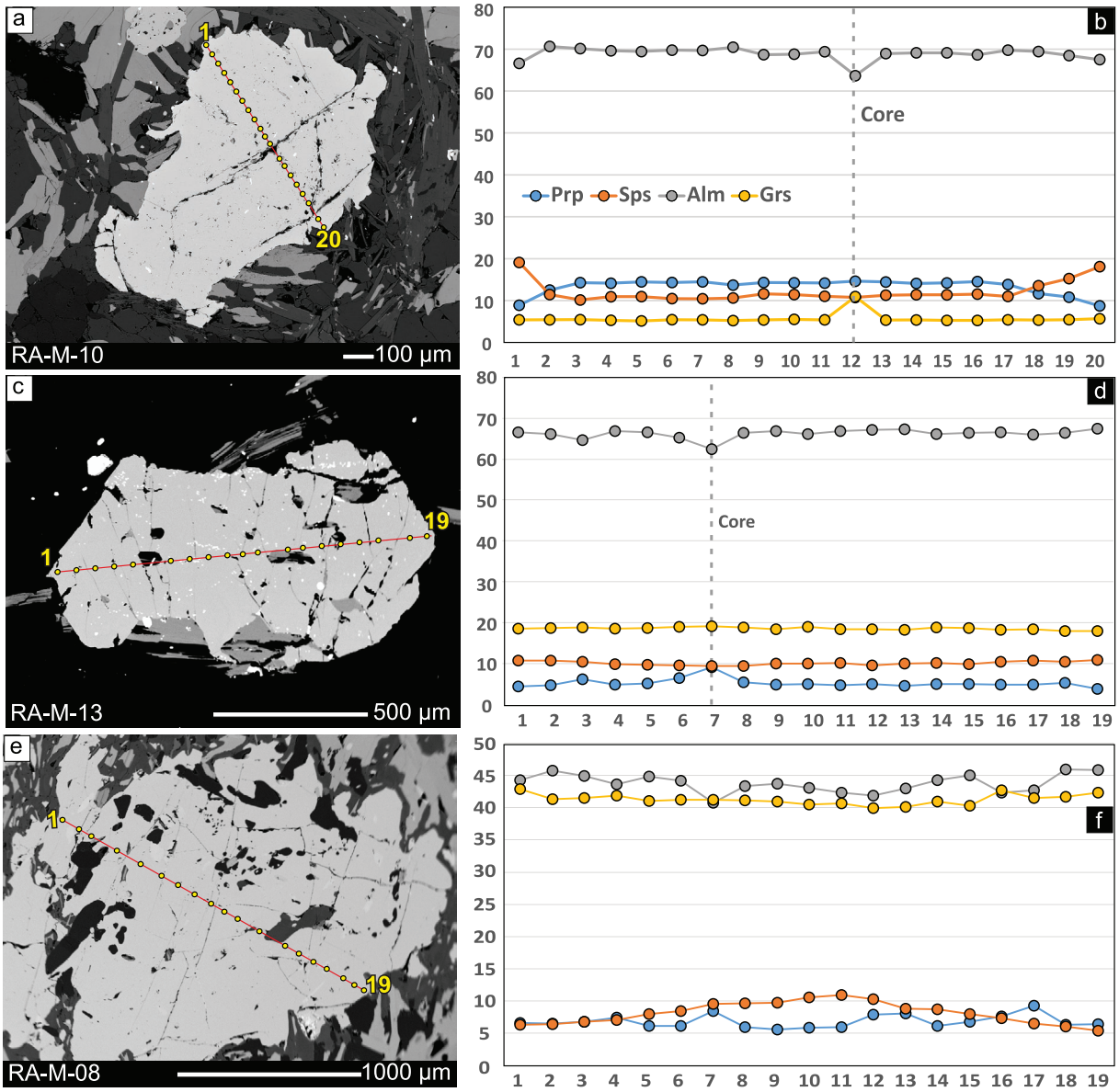


Fig. 4. Compositional profiles of garnet: **(a)** BSE image of representative garnet porphyroblast from sample RA–M–10 with marked profile line and spots. **(b)** Compositional profiles of garnet end members from the same sample RA–M–10. **(c)** BSE image of representative garnet porphyroblast from sample RA–M–13 with marked profile line and spots. **(d)** Compositional profiles of garnet end members from the same sample RA–M–13. **(e)** BSE image of representative garnet porphyroblast from sample RA–M–08 with marked profile line and spots. **(f)** Compositional profiles of garnet end members from the same sample RA–M–08.

Sample RA–M–10

The P–T conditions of the inferred maximum burial (M0) stage at 820 MPa and 680 °C are given by sample RA–M–10 for garnet-supposed core composition (Xprp=15, Xgrs=11, Xsps=11 mol.%) (Fig. 4a,b) in the Bt, Grt, Ilm, Ms, Plg, Rt stability field (Fig. 7). The crossing or proximity of garnet mantle isopleths composition, with values of Xprp=14, Xgrs=5, and Xsps=12 mol.%, indicates similar temperature conditions of 680 °C and slightly lower pressure of 700 MPa for stage M1. This change from core to mantle is primarily due to the decrease in the grossular component. Retrogressed values of garnet rim composition (Xprp=9, Xgrs=5, Xsps=18 mol.%) show conditions of 570 °C at 570 MPa within the stability field of Bt, Grt, Chl, Ms, Ilm, Plg, Qtz, Rt mineral assemblage for stage M2. All calculated P–T values suggest a clockwise P–T path for sample RA–M–10 (Fig. 7).

Sample RA–M–41

Like sample RA–M–10, similar conditions were modelled for sample RA–M–41 when taking into consideration its inferred core composition of Xprp=10 mol.%, Xgrs=8–9 mol.%, and Xsps=1–2 mol.%. The modelled isopleths crossed inside

Table 3: EPMA biotite mineral chemistry for sample RA–M–10.

Mineral/An. No.	Bt/5	Bt/6	Bt/13	Bt/14	Bt/16	Bt/23	Bt/24	Bt/27	Bt/28	Bt/45	Bt/46	Bt/49
SiO_2 (wt.%)	35.36	35.88	34.97	35.52	35.74	35.35	34.73	34.66	34.62	34.94	36.13	35.15
TiO_2	1.79	1.68	2.20	2.23	1.58	1.43	1.30	1.66	1.72	1.40	1.66	1.83
Al_2O_3	19.01	18.77	18.70	18.86	19.18	18.92	19.39	19.26	19.35	19.93	19.53	19.78
FeO	19.01	18.82	18.85	18.65	18.73	18.67	19.20	19.10	19.15	19.07	18.97	18.63
MnO	0.23	0.29	0.20	0.23	0.27	0.22	0.20	0.24	0.22	0.25	0.23	0.21
MgO	9.56	9.77	9.37	9.50	9.77	9.73	9.52	9.46	9.59	9.85	9.96	9.63
CaO	0.00	0.03	0.00	0.02	0.01	0.03	0.04	0.00	0.01	0.00	0.02	0.03
Na_2O	0.15	0.10	0.19	0.16	0.17	0.13	0.18	0.16	0.20	0.14	0.14	0.18
K_2O	9.50	9.66	9.43	9.37	9.46	9.36	9.28	9.60	9.58	9.48	9.56	9.48
H_2O	3.91	3.93	3.88	3.92	3.94	3.89	3.88	3.88	3.89	3.93	3.99	3.94
Total	**98.52**	**98.93**	**97.82**	**98.46**	**98.85**	**97.73**	**97.71**	**97.96**	**98.32**	**98.98**	**100.20**	**98.87**
Si *(a.p.f.u)*	5.42	5.47	5.40	5.43	5.44	5.45	5.37	5.36	5.33	5.33	5.43	5.36
Al iv	2.58	2.53	2.60	2.57	2.56	2.55	2.63	2.64	2.67	2.67	2.57	2.64
Al vi	0.85	0.84	0.81	0.83	0.89	0.89	0.91	0.87	0.84	0.91	0.89	0.91
Ti	0.21	0.19	0.26	0.26	0.18	0.17	0.15	0.19	0.20	0.16	0.19	0.21
Fe	2.44	2.40	2.44	2.39	2.39	2.41	2.48	2.47	2.47	2.43	2.38	2.37
Mn	0.03	0.04	0.03	0.03	0.03	0.03	0.03	0.03	0.03	0.03	0.03	0.03
Mg	2.18	2.22	2.16	2.17	2.22	2.24	2.19	2.18	2.20	2.24	2.23	2.19
Ca	0.00	0.00	0.00	0.00	0.00	0.01	0.01	0.00	0.00	0.00	0.00	0.00
Na	0.04	0.03	0.06	0.05	0.05	0.04	0.05	0.05	0.06	0.04	0.04	0.05
K	1.86	1.88	1.86	1.83	1.84	1.84	1.83	1.89	1.88	1.84	1.83	1.84
OH	4.00	4.00	4.00	4.00	4.00	4.00	4.00	4.00	4.00	4.00	4.00	4.00
Total	**19.61**	**19.60**	**19.60**	**19.55**	**19.60**	**19.61**	**19.65**	**19.67**	**19.68**	**19.66**	**19.59**	**19.61**
Y total	**5.71**	**5.69**	**5.68**	**5.67**	**5.71**	**5.72**	**5.76**	**5.73**	**5.74**	**5.78**	**5.72**	**5.71**
X total	**1.90**	**1.91**	**1.91**	**1.88**	**1.89**	**1.88**	**1.89**	**1.94**	**1.94**	**1.89**	**1.88**	**1.90**
Al total	**3.43**	**3.37**	**3.41**	**3.40**	**3.44**	**3.44**	**3.53**	**3.51**	**3.51**	**3.58**	**3.46**	**3.55**
Fe/(Fe+Mg)	0.53	0.52	0.53	0.52	0.52	0.52	0.53	0.53	0.53	0.52	0.52	0.52
Mg/(Mg+Fe)	0.47	0.48	0.47	0.48	0.48	0.48	0.47	0.47	0.47	0.48	0.48	0.48

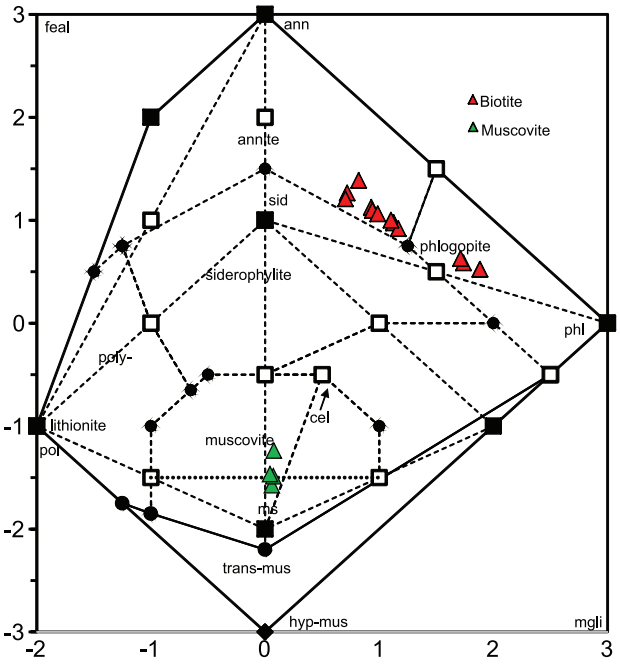


Fig. 5. Classification diagram (after Tischendorf et al. 2007) for biotite and muscovite from sample RA–M–10.

the stability field of Bt, Gt, Ilm, Ms, Plg, and St reaching 780–820 MPa and 640–670 °C, which is inferred to be the maximum burial (M0) stage (Fig. 8). Unfortunately, the retrograde zoning in the composition from core to rim is hardly distinguishable in RA–M–41 (up to 2 mol.%; Table 8), especially in the pyrope and spessartine component; therefore, we were not able to determine other stages or draw any P–T path similar to sample RA–M–10.

An additional source of uncertainty in the pseudosection modelling is related to the progressive growth of compositionally zoned garnet, which may modify the effective bulk-rock composition through sequestration of Fe, Mg, Mn, and Ca during prograde metamorphism. Such fractionation can influence the positions of mineral stability fields and consequently the calculated P–T estimates (Evans 2004; Diener et al. 2008; Gaidies et al. 2008). In the present study, pseudosections were constructed using measured whole-rock compositions and therefore do not explicitly account for changes in effective bulk composition during garnet growth. However, the majority of garnet porphyroblasts are relatively small (typically 0.5–2 mm in diameter) and occur in comparatively low modal abundances, thereby suggesting that fractionation effects were likely insufficient to significantly modify the positions of major assemblage fields. Furthermore, the calculated peak metamorphic conditions correspond with previously published thermobarometric estimates from the KMC (Searle et al. 2010;

Table 4: EPMA muscovite mineral chemistry for sample RA–M–10.

Mineral/An. No.	Ms/8	Ms/9	Ms/19	Ms/30
SiO_2 (wt.%)	45.60	45.74	46.07	45.35
TiO_2	1.12	1.01	0.43	0.70
Al_2O_3	34.06	34.33	35.47	35.32
FeO	1.25	1.20	0.99	1.18
MnO	0.02	0.04	0.03	0.00
MgO	0.94	0.81	0.68	0.66
CaO	0.00	0.00	0.01	0.01
Na_2O	0.57	0.56	0.60	0.50
K_2O	10.65	10.74	10.60	10.73
H_2O	4.44	4.45	4.49	4.46
Total	**98.65**	**98.87**	**99.35**	**98.91**
Si *(a.p.f.u)*	6.158	6.161	6.153	6.102
Aliv	1.842	1.839	1.847	1.898
Alvi	3.579	3.612	3.738	3.703
Ti	0.114	0.102	0.043	0.070
Fe	0.141	0.135	0.110	0.133
Mn	0.002	0.004	0.003	0.000
Mg	0.189	0.162	0.135	0.133
Na	0.149	0.146	0.155	0.132
K	1.835	1.846	1.806	1.842
OH	4	4	4	4
Total	**18**	**18**	**18**	**18**
Y total	**4.03**	**4.02**	**4.03**	**4.04**
X total	**1.98**	**1.99**	**1.96**	**1.97**
Al total	**5.42**	**5.45**	**5.58**	**5.60**
Fe/(Fe+Mg)	0.43	0.45	0.45	0.50
Mg/(Mg+Fe)	0.57	0.53	0.56	0.50

Table 5: EPMA plagioclase mineral chemistry for sample RA–M–10.

Mineral/An. No.	Plg/10	Plg/11	Plg/20	Plg/21	Plg/31	Plg/32
SiO_2 (wt.%)	62.05	61.51	62.08	61.92	62.29	62.96
TiO_2	0.00	0.00	0.00	0.00	0.00	0.00
Al_2O_3	24.11	23.79	24.03	24.27	24.27	24.38
FeO	0.08	0.02	0.09	0.13	0.04	0.02
MnO	0.00	0.00	0.00	0.00	0.00	0.00
MgO	0.00	0.01	0.00	0.02	0.01	0.00
CaO	5.41	5.46	5.49	5.51	5.38	5.33
Na_2O	8.21	8.10	8.13	7.99	8.21	8.22
K_2O	0.15	0.11	0.18	0.13	0.19	0.13
Total	**100.01**	**99.00**	**100.00**	**99.97**	**100.37**	**101.05**
Oxygen p.f.u.	**8**	**8**	**8**	**8**	**8**	**8**
Si *(a.p.f.u)*	2.748	2.751	2.750	2.742	2.748	2.755
Al	1.258	1.254	1.255	1.267	1.262	1.258
Fe	0.003	0.001	0.003	0.005	0.001	0.001
Mg	0.000	0.000	0.000	0.001	0.000	0.000
Ca	0.257	0.261	0.261	0.262	0.254	0.250
Na	0.705	0.703	0.698	0.686	0.703	0.697
K	0.008	0.006	0.010	0.007	0.010	0.007
Total	**5**	**5**	**5**	**5**	**5**	**5**
An	0.26	0.27	0.27	0.27	0.26	0.26
Ab	0.73	0.72	0.72	0.72	0.73	0.73
Or	0.01	0.01	0.01	0.01	0.01	0.01
X_{Ca}	0.27	0.27	0.27	0.27	0.27	0.27

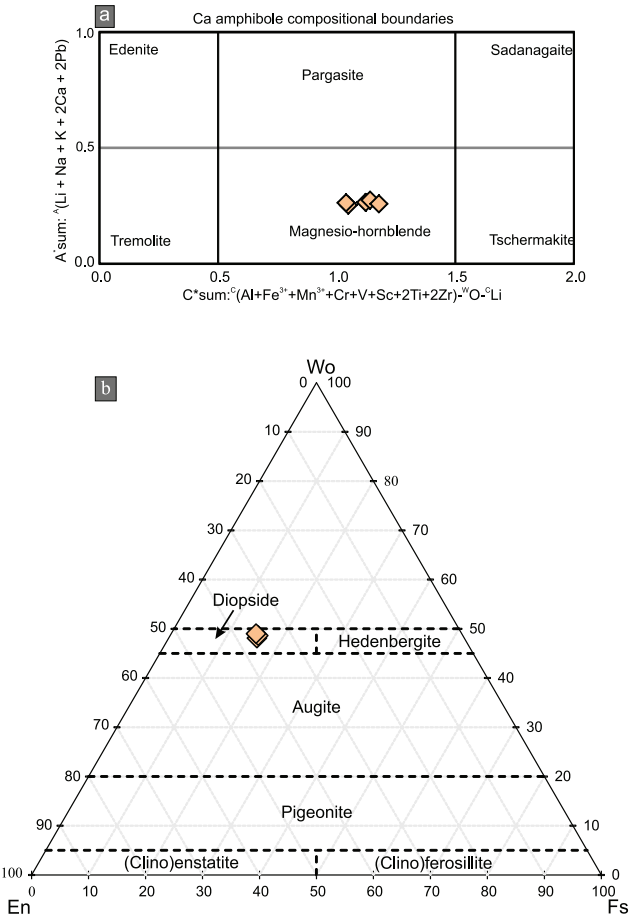


Fig. 6. Amphibole and clinopyroxene classifications for sample RA–M–08 (Grt–Cpx–Hbd orthogeniss): **(a)** magnesio–hornblende (Mg–Hbd) amphibole from Hawthorne et al. (2012); **(b)** diopside end-member from Morimoto et al. (1988).

Palin et al. 2012). Therefore, although progressive garnet fractionation may introduce some uncertainty into the modelling results, it is unlikely to affect the principal interpretation of a clockwise P–T evolution documented in the studied rocks.

Discussion and interpretations

Tectonic implications

The studied metamorphic history of amphibolite facies rocks in the Hunza Valley corresponds to the Eocene collision of the Indian plate with the Eurasian plate along the MKT (Ahmad et al. 2025). The metamorphic history of the studied samples is linked to the N–S directed India–Kohistan Island Arc–Asia collision recently dated at 47±4.3 Ma (Ahmad et al. 2025).

On a larger scale within the Hunza region, Fraser et al. (2001) and Palin et al. (2012) recognised four distinct metamorphic events (M0, M1, M2 and M3) dated at 105.5±0.8 Ma

Table 6: EPMA amphibole analyses from sample RA–M–08.

Mineral/An. No.	Amp/2	Amp/3	Amp/4	Amp/10	Amp/11
SiO2 (wt.%)	43.78	43.82	43.66	44.87	44.53
TiO2	0.93	0.71	0.51	0.89	0.84
Al2O3	11.82	11.66	11.55	10.80	11.02
FeO	16.13	16.50	16.07	16.37	16.74
CaO	11.75	11.86	11.50	11.91	11.94
Na2O	1.08	1.08	1.11	1.02	1.02
K2O	0.00	0.00	0.00	0.00	0.00
MnO	0.37	0.39	0.47	0.44	0.43
MgO	8.85	9.32	9.59	9.62	9.09
Cl	0.03	0.00	0.00	0.02	0.03
F	0.14	0.00	0.00	0.16	0.13
Initial Total	**94.88**	**95.35**	**94.45**	**96.10**	**95.76**
Mn_2O_3	0.00	0.00	0.00	0.00	0.00
FeO	15.35	14.42	13.43	14.95	15.68
Fe_2O_3	0.87	2.31	2.93	1.58	1.18
H_2O+	1.90	1.98	1.97	1.91	1.91
Total	**96.96**	**97.65**	**96.94**	**98.22**	**97.88**
Si *(a.p.f.u)*	6.668	6.627	6.632	6.743	6.733
Al	1.332	1.373	1.368	1.257	1.267
Ti	0.000	0.000	0.000	0.000	0.000
ΣT	**8**	**8**	**8**	**8**	**8**
Ti	0.106	0.081	0.058	0.100	0.096
Al	0.789	0.705	0.700	0.656	0.696
V	0.000	0.000	0.000	0.000	0.000
Cr	0.000	0.000	0.000	0.000	0.000
Fe^{3+}	0.100	0.263	0.335	0.179	0.134
Ni	0.000	0.000	0.000	0.000	0.000
Zn	0.000	0.000	0.000	0.000	0.000
Mn^{2+}	0.020	0.014	0.000	0.018	0.024
Fe^{2+}	1.955	1.824	1.707	1.878	1.983
Mg	2.009	2.155	2.049	2.102	2.173
ΣC	**5**	**5**	**5**	**5**	**5**
Mn^{2+}	0.028	0.036	0.060	0.038	0.031
Fe^{2+}	0.000	0.000	0.000	0.000	0.000
Mg	0.000	0.000	0.000	0.000	0.000
Ca	1.917	1.922	1.872	1.918	1.934
Na	0.054	0.042	0.068	0.044	0.035
ΣB	**2**	**2**	**2**	**2**	**2**
Na	0.264	0.274	0.258	0.252	0.263
K	0.000	0.000	0.000	0.000	0.000
ΣA	**0.264**	**0.274**	**0.258**	**0.252**	**0.263**
O (non-W)	**22**	**22**	**22**	**22**	**22**
OH	1.925	2.000	2.000	1.918	1.931
F	0.067	0.000	0.000	0.076	0.062
Cl	0.008	0.000	0.000	0.006	0.007
O	0.000	0.000	0.000	0.000	0.000
ΣW	**2**	**2**	**2**	**2**	**2**
Σ T,C,B,A	**15.24**	**15.32**	**15.11**	**15.19**	**15.37**

Mn_2O_3, was estimated by charge balance during structural formula recalculation.

Table 7: EPMA clinopyroxene analyses from sample RA–M–08.

Mineral/An. No.	Cpx/1	Cpx/8	Cpx/9
SiO_2 (wt.%)	53.27	52.62	52.82
TiO_2	0.06	0.03	0.04
Al_2O_3	0.71	0.78	0.57
Cr_2O_3	0.05	0.03	0.02
FeO	12.85	12.29	11.49
MnO	0.45	0.57	0.52
MgO	10.29	9.98	10.44
CaO	23.03	22.99	23.28
Na_2O	0.27	0.29	0.28
Σ	**100.97**	**99.56**	**99.47**
Si *(a.p.f.u)*	1.966	1.955	1.947
Al	0.034	0.045	0.053
Mg	0.671	0.664	0.653
Ca	0.944	0.923	0.932
Na	0.033	0.039	0.040
Ti	0.001	0.000	0.005
Fe^{3+}	0.010	0.022	0.033
Fe^{2+}	0.262	0.252	0.258
Mn	0.000	0.000	0.000
Cr	0.001	0.002	0.002
Σ	**4**	**4**	**4**
Wo	49	48	49
En	36	36	36
Fs	15	15	15

(M0), 44.0±2.0 Ma (M1) and 28.2±0.8 Ma (M2). The younger M3 event is dated at 16.0±1.0 Ma south of the Hassanabad thrust (cf. Palin et al. 2012). Sayab et al. (2021) studied spiral garnets in a sample from the same region (lower sillimanite zone of Palin et al. 2012) and interpreted three growth stages (stage-I, stage-II, stage-III) associated with early andalusite grade metamorphism (M0) overprinted by later sillimanite (M1) accompanied by a succession of horizontal and vertical foliations . However, they were uncertain about whether gravitational collapse during stage-II growth was responsible for a major decompression and the resulting sillimanite growth in the region or that decompression predates stage-II garnet growth. The age assigned to peak sillimanite grade metamorphism in the Hunza Valley by Fraser et al. (2001) is 44.0±2.0 Ma (U–Pb monazite), which corresponds with the U–Th–Pb monazite age of 47±4.3 Ma of Ahmad et al. (2025). These ages could correspond to the initiation of decompression in the Hunza Valley. These overlapping Eocene monazite ages likely record the culmination of peak metamorphism and the onset of near-isothermal decompression following crustal thickening during the India–Asia collision. They mark the transition from crustal burial to tectonic exhumation, when pressure decreased while temperatures remained sufficiently high to stabilise sillimanite, thus reflecting the initial uplift and tectonic exhumation of the thickened Asian crust (e.g., Palin et al. 2012; Stübner et al. 2014; Khanal et al. 2021; Ahmad et al. 2025).

Age and tectonic significance of the P–T path

Garnet core to rim isopleth intersections plotted on the P–T pseudosection of sample RA–M–10 identify episodic garnet formation along a clockwise P–T path. P–T pseudosections were constructed in the MnNCKFMASHTO chemical system and the geothermobarometry of garnet core, mantle and rim

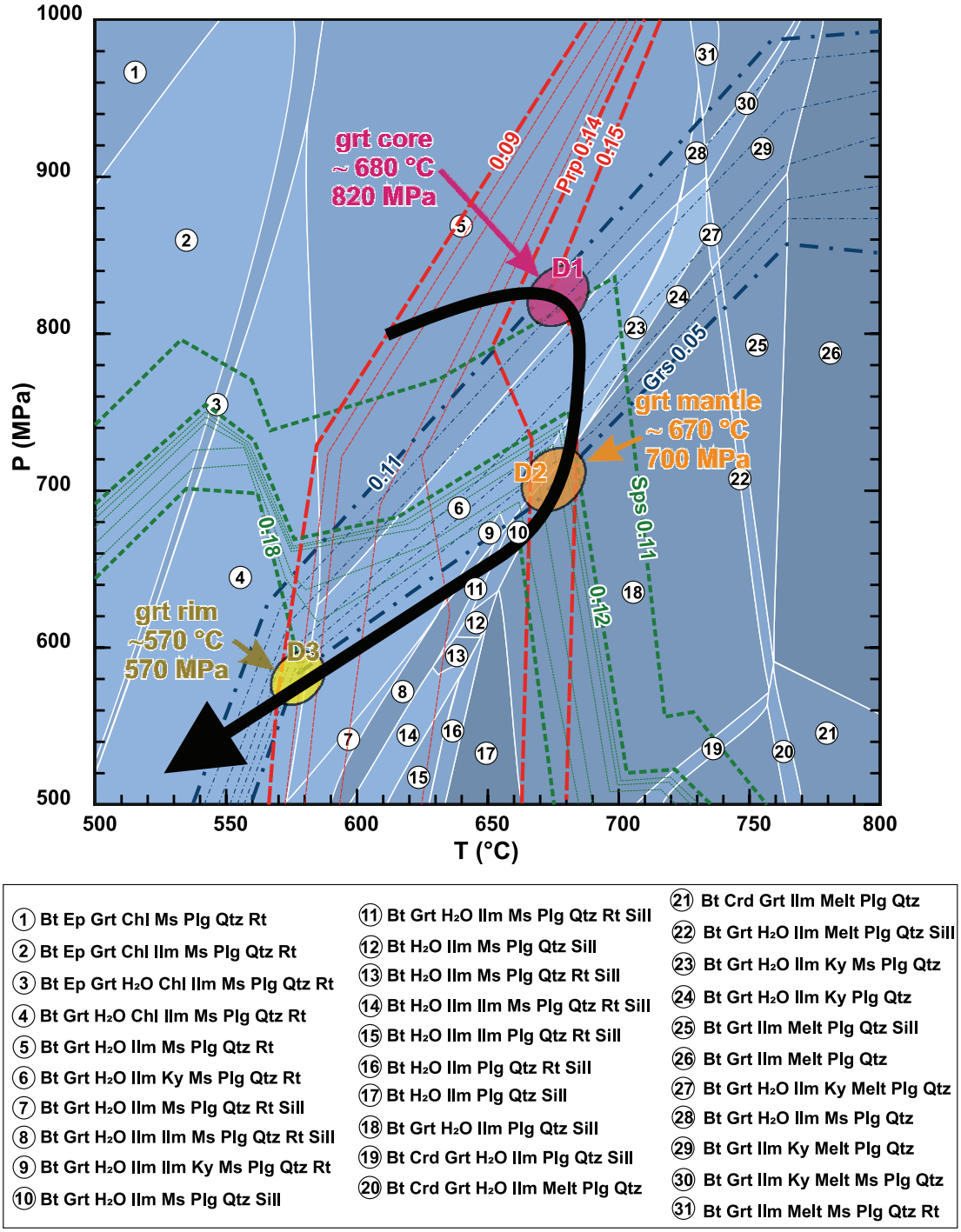


Fig. 7. Pseudosection of sample RA–M–10 with isopleths of garnet core, mantle and rim composition creating a clockwise P–T path. Grt core composition isopleths are crossing at the P–T conditions of the inferred maximum burial (M0) stage at 820 MPa and 680 °C.

isopleths, along with the sequential development of garnet, muscovite, and biotite delineates the clockwise P–T–t–D path for studied sample RA–M–10, which is also compatible with peak conditions inferred for sample RA–M–41. In sample RA–M–10, garnet end members isopleths intersection for core, mantle, and rim vary in temperature from 680 °C, 670 °C, and 570 °C and pressure from 820 kbar, 700 kbar and 570 MPa respectively. Based on the garnet compositional zoning (Fig. 4a–e) and pseudosection interpretation, we distinguish three principal stages of metamorphic evolution: (i) D1 prograde metamorphism culminating in peak P–T conditions of 820 MPa at 680 °C and growth of garnet cores, (ii) D2 near-isothermal decompression at ca. 670 °C and 700 MPa during the initial stages of exhumation recorded by garnet

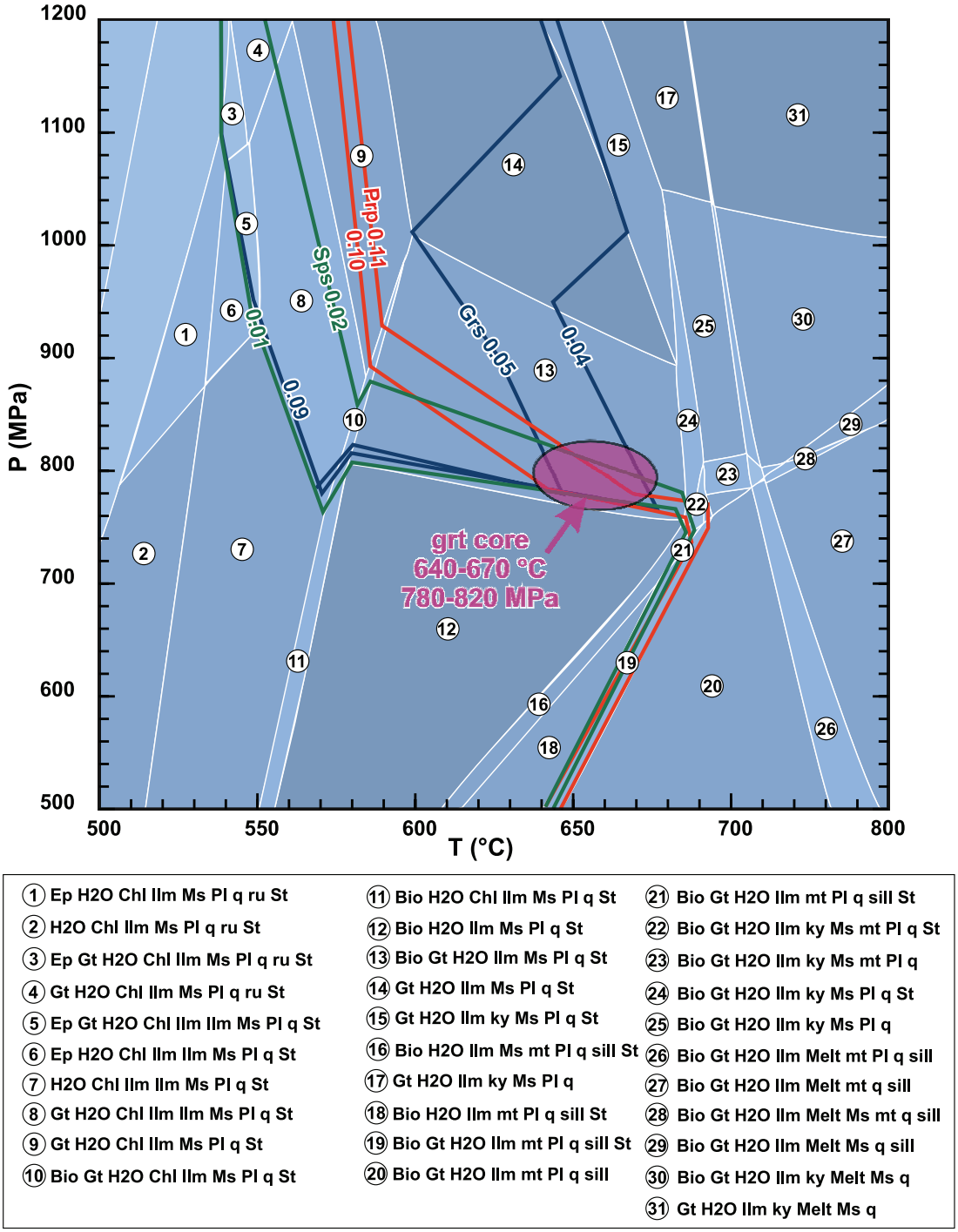


Fig. 8. Pseudosection of sample RA–M–41 with isopleths of garnet core composition crossing at the P–T conditions of the inferred maximum burial (M0) stage at 780–820 MPa and 640–670 °C.

mantle compositions, and (iii) D3 uplift and cooling associated with retrograde evolution at 570 MPa and 570 °C. Overall, peak P–T conditions in the Hunza Valley from KMC samples in this study fall between ~780–820 MPa and ~640–680 °C (Figs. 7, 8). The P–T trajectory (Fig. 7) indicates that peak metamorphic conditions were attained during D1-related garnet growth. Subsequent exhumation was accompanied by near-isothermal decompression recorded by the transition from garnet core to mantle compositions (Fig. 4a–e). Such decompression is consistent with rapid exhumation of previously thickened crust following continental collision. The near-isothermal character of this stage may reflect exhumation under a persistently elevated geothermal regime associated with syn- to late-tectonic magmatism and emplacement of granitoid

Table 8: Modified whole rock composition of samples RA–M–10 and RA–M–41 used for the P–T modeling.

Oxides (wt.%)	RA–M–10	RA–M–41
SiO_2	66.46	47.61
TiO_2	0.86	0.95
Al_2O_3	14.50	33.30
FeO	5.59	12.00
MnO	0.09	0.05
MgO	2.68	1.54
CaO	2.74	0.83
Na_2O	3.23	0.62
K_2O	2.50	1.54
P_2O_5	0.22	0.49
LOI	1.15	3.84
Oxides (mol.%)	**RA–M–10**	**RA–M–41**
SiO_2	69.36	49.9
TiO_2	0.67	0.75
Al_2O_3	8.92	20.57
FeO	4.88	10.52
MnO	0.08	0.04
MgO	4.17	2.41
CaO	2.75	0.22
Na_2O	3.27	0.63
O_2	0.24	0.52
H_2O	in excess	in excess

bodies within the KMC and adjacent Baltoro region (Fraser et al. 2001; Foster et al. 2004; Searle et al. 2010; Palin et al. 2012). Continued uplift subsequently resulted in cooling and development of the retrograde mineral assemblages associated with D3 deformation. However, the studied samples do not provide unequivocal petrographic evidence for a distinct reheating event or a separate generation of garnet growth directly related to intrusion emplacement.

Overall, peak P–T conditions in the Hunza Valley deduced from our KMC samples fall between ~780–820 MPa and ~640–680 °C. These conditions are consistent with ~7.4–8.0 kbar and ~640–660 °C (Palin et al. 2012) and 7.7±1.8 kbar and 648±30 °C (Searle et al. 2010). Garnet core isopleths intersection in the Bt, Grt, Ilm, Ms, Plg, Rt field and Bt, Gt, Ilm, Ms, Plg and St field and muscovite and biotite inclusions in garnet porphyroblasts indicate that biotite and muscovite predate garnet growth. Biotite, quartz, muscovite, ilmenite and rutile inclusions in garnet porphyroblast, garnet core isopleth intersections at ~780–820 MPa and ~640–680 °C dated as c. 47±4.3 Ma (U–Pb monazite; Ahmad et al. 2025) suggest that amphibolite facies metamorphism along the southern edge of the Eurasian plate is related to the Early–Middle Eocene N–S collision of India with the Kohistan Arc previously assembled with Eurasia. Estimated pressure of ~7.8 kbar at 28.2±0.8 Ma (Palin et al. 2012), ~6 kbar at 553±23 °C around ~82 Ma (Foster et al. 2004) and ~8 kbar deduced herein around 47±4.3 Ma suggest long-lived residence of the studied rocks at a depth of approximately 20 to 21 km, followed by fast exhumation in the late Oligocene to Miocene.

Conclusions

Well-developed garnet porphyroblasts preserve continuous S_1 inclusion trails that are truncated by the main matrix S_2 foliation, whereas the S_3 foliation overprints both earlier fabrics. These structural relationships record a progressive, polyphase deformation history and provide new constraints on a very complex tectonic history on the southern margin of the Eurasian/Asian plate.

Geothermobarometric analysis and modelling of garnet core, mantle, and rim compositions, in combination with evidence for sequential crystallisation of garnet, muscovite, and biotite define a clockwise P–T path for the two studied samples (RA–M–10 and RA–M–41) from the Hunza valley in the KMC, North Pakistan. Peak P–T conditions determined in this study range from approximately 780 to 820 MPa and 640 to 680 °C.

Multiple metamorphic stages identified by previous researchers, along with the findings of this study regarding P–T paths and published geochronological evidence from the southern Karakoram plate margin, indicate that the southern Karakoram plate margin experienced a prolonged and episodic tectonometamorphic evolution. These data suggest that crustal thickening during continental convergence was followed by successive phases of deformation, including upright folding, regional doming, and localised extensional exhumation. These changes likely reflect the redistribution of strain during the late stages of orogenesis, when partially molten middle crust was uplifted in response to gravitational collapse and tectonic unroofing.

Acknowledgments: The authors acknowledge the Department of Geology, University of Peshawar for logistic support to conduct the field work for data and samples collection. We are also thankful to the Higher Education Commission (HEC) of Pakistan and the Slovak Academic Information Agency (SAIA) Slovakia for providing opportunities to the first author to conduct different analyses in state-of-the-art laboratories. This work was supported by the EU NextGenerationEU through Slovakia Recovery and Resilience Plan under the project No. 09I03-03-V04-00071 and Ministry of Education, Research, Development and Youth of the Slovak Republic under VEGA-1/0028/24 project. The authors sincerely thank the two reviewers for their constructive comments and valuable suggestions, which significantly helped improve the quality and clarity of this manuscript.

References

Aerden D.G.A.M. 1998: Tectonic evolution of the Montagne Noire and possible orogenic model for syn-collisional exhumation of deep rocks, Hercynian belt, France. *Tectonics* 17, 62–79. https://doi.org/10.1029/97TC02342

Aerden D.G.A.M. & Ruiz-Fuentes A. 2020: X-ray computed microtomography of spiral garnets: A new test of how they form. *Journal of Structural Geology* 136, 104054. https://doi.org/10.1016/j.jsg.2020.104054

Ahmad R., Ali A., Nemec O., Putiš M. & Konečný P. 2025: Geochronological constraints on the Karakoram Metamorphic Complex, Hunza Valley, Pakistan: Zircon and monazite dating of Tethyan collision events. *Geologica Carpathica* 76, 23–36. https://doi.org/10.31577/GeolCarp.2025.02

Ali A. 2010: The tectono-metamorphic evolution of the Balcooma Metamorphic Group, north-eastern Australia: a multidisciplinary approach. *Journal of Metamorphic Geology* 28, 397–422. https://doi.org/10.1111/j.1525-1314.2010.00871.x

Ali A., Habib U., Rehman U.A., Zada N., Abidin U.Z. & Ismail M. 2016: Tectonic Imprints of the Hazara Kashmir Syntaxis on the Mesozoic Rocks Exposed in Munda, Mohmand Agency, Northwest Pakistan. *Acta Geologica Sinica* 90, 440–455. https://doi.org/10.1111/1755-6724.12682

Bell T.H. & Rubenach M.J. 1983: Sequential porphyroblast growth and crenulation cleavage development during progressive deformation. *Tectonophysics* 92, 171–194. https://doi.org/10.1016/0040-1951(83)90089-6

Bell T.H., Hickey K.A. & Upton J.G. 1998: Distinguishing and correlating multiple phases of metamorphism across a multiply re-gion using the axes of spiral, staircase and sigmoidal inclusion trails in garnet. *Journal of Metamorphic Geology* 16, 767–794. https://doi.org/10.1111/j.1525-1314.1998.00170.x

Berry R.F., Steele D.A. & Meffre S. 2008: Proterozoic metamorphism in Tasmania: implications for tectonic reconstructions. *Precambrian Research* 166, 387–396. https://doi.org/10.1016/j.precamres.2007.05.004

Borneman N.L., Hodges K.V., van Soest M.C., Bohon W., Wartho J.-A., Cronk S.S. & Ahmad T. 2015: Age and structure of the Shyok suture in the Ladakh region of northwestern India: Implications for slip on the Karakoram fault system. *Tectonics* 34, 2011–2033. https://doi.org/10.1002/2015TC003933

Brandon C. & Romanowicz B. 1986: A "no-lid" zone in the central Chang-Thang platform of Tibet: Evidence from pure path phase velocity measurements of long period Rayleigh waves. *Journal of Geophysical Research* 91, 6547–6564. https://doi.org/10.1029/JB091iB06p06547

Christie D.M., Carmichael I.S. & Langmuir C.H. 1986: Oxidation states of mid-ocean ridge basalt glasses. *Earth and Planetary Science Letters* 79, 397–411. https://doi.org/10.1016/0012-821X(86)90195-0

Connolly J.A.D. 1990: Multivariable phase-diagrams – an algorithm based on generalised thermodynamics. *American Journal of Science* 290, 666–718. https://doi.org/10.2475/ajs.290.6.666

Connolly J.A.D. 2005: Computation of phase equilibria by linear programming: a tool for geodynamic modeling and its application to subduction zone decarbonation. *Earth and Planetary Science Letters* 236, 524–541. https://doi.org/10.1016/j.epsl.2005.04.033

Connolly J.A.D. & Petrini K. 2002: An automated strategy for calculation of phase diagram sections and retrieval of rock properties as a function of physical conditions. *Journal of Metamorphic Geology* 20, 697–708. https://doi.org/10.1046/j.1525-1314.2002.00398.x

Cottle J.M., Searle M.P., Horstwood M.S.A. & Waters D.J. 2009: Timing of midcrustal metamorphism, melting and deformation in the Mount Everest Region of Southern Tibet revealed by U–(Th)–Pb geochronology. *Journal of Geology* 117, 643–664. https://doi.org/10.1086/605994

Crawford M.B. & Searle M.P. 1993: Collision–related granitoid magmatism and crustal structure of the Hunza Karakoram, north Pakistan. *Geological Society London, Special Publications* 74, 53–68. https://doi.org/10.1144/GSL.SP.1993.074.01.05

Diener J.F.A., Powell R., White R.W. & Holland T.J.B. 2008: A new thermodynamic model for clino- and orthoamphiboles in Na_2O–CaO–FeO–MgO–Al_2O_3–SiO_2–H_2O–O systems. *Journal of Metamorphic Geology* 26, 631–656. https://doi.org/10.1111/j.1525-1314.2007.00720.x

Evans T.P. 2004: A method for calculating effective bulk composition modification due to crystal fractionation in garnet-bearing schist: implications for isopleth thermobarometry. *Journal of Metamorphic Geology* 22, 547–557. https://doi.org/10.1111/j.1525-1314.2004.00532.x

Foster G., Parrish R.R., Horstwood M., Chenery S., Pyle J. & Gibson H.D. 2004: The generation of prograde P–T–t points and paths; a textural, compositional and chronological study of metamorphic monazite. *Earth and Planetary Science Letters* 228, 125–142. https://doi.org/10.1016/j.epsl.2004.09.024

Fraser J.E., Searle M.P., Parrish R.R. & Noble S.R. 2001: Chronology of deformation, metamorphism, and magmatism in the southern Karakoram Mountains. *Geological Society of America Bulletin* 113, 1443–1455. https://doi.org/10.1130/0016-7606(2001)113%3C1443:CODMAM%3E2.0.CO;2

Gaidies F., de Capitani C. & Abart R. 2008: THERIA_G: a software program to numerically model prograde garnet growth. *Contributions to Mineralogy and Petrology* 155, 657–671. https://doi.org/10.1007/s00410-007-0263-z

Gan W., Zhang P., Shen Z.–H., Niu Z., Wang M., Wan Y., Zhou D. & Cheng, J. 2007: Present–day crustal motion within the Tibetan Plateau inferred from GPS measurements. Journal of *Geophysical Research* 112, B08416. https://doi.org/10.1029/ 2005JB004120

Guevara V.E., Smye A.J., Caddick M.J., Searle M.P., Olsen T., Whalen L., Kylander-Clark A.R., Jercinovic M.J., Waters D.J. 2022: A modern pulse of ultrafast exhumation and diachronous crustal melting in the Nanga Parbat Massif. *Science Advances* 8, 1–15. https://doi.org/10.1126/sciadv.abm2689

Hawthorne F., Oberti R., Harlow G., Maresch W., Martin R.F., Schumacher J. & Welch M. 2012: Nomenclature of the amphibole supergroup. IMA report, *American Mineralogist* 97, 2031–2048. https://doi.org/10.2138/am.2012.4276

Holland T. & Powell R. 2003: Activity–composition relations for phases in petrological calculations: an asymmetric multicomponent formulation. *Contributions to Mineralogy and Petrology* 145, 492–501. https://doi.org/10.1007/s00410-003-0464-z

Holland T.J.B. & Powell R. 2011: An improved and extended internally consistent thermodynamic dataset for phases of petrological interest, involving a new equation of state for solids. *Journal of Metamorphic Geology* 29, 333–383. https://doi.org/10.1111/j.1525-1314.2010.00923.x

Hussain A., Zhao K.D., Rehman H.U., Sadiq I., Li Q., Baig S.S. & Ullah I. 2024: Geochronology and petrogenesis of the Miocene S–type Sumayar granite in the Karakoram Block, north Pakistan: Implications for post–collisional magmatism. *Journal of Asian Earth Sciences* 264, 106053. https://doi.org/10.1016/j.jseaes.2024.106053

Khanal G.P., Wang J.M., Larson K.P., Wu F.Y., Rai S.M., Wang J.G. & Yang L. 2021: Eocene metamorphism and anatexis in the Kathmandu Klippe, Central Nepal: Implications for early crustal thickening and initial rise of the Himalaya. *Tectonics* 40, e2020TC006532. https://doi.org/10.1029/2020TC006532

Larson K.P., Ali A., Shrestha S., Soret M., Cottle J.M. & Ahmad R. 2019: Timing of metamorphism and deformation in the Swat valley, northern Pakistan: Insight into garnet-monazite HREE partitioning. *Geoscience Frontiers* 10, 849–861. https://doi.org/10.1016/j.gsf.2018.02.008

Le Fort P., Lemennicier Y., Lombardo B., Pêcher A., Pertusati P., Pognante U. & Rolfo F. 1995: Preliminary geological map and description of the Himalaya-Karakorum junction in Chogo Lungma to Turmik area (Baltistan, northern Pakistan). *Journal of the Geological Society of Nepal Special Issue* 11, 17–38.

Lemennicier Y., Le Fort P., Lombardo B., Pêcher A. & Rolfo F. 1996: Tectonometamorphic evolution of the central Karakorum (Baltistan – northern Pakistan). *Tectonophysics* 260, 119–143. https://doi.org/10.1016/0040-1951(96)00080-7

Morimoto N., Fabries J., Ferguson A.K., Ginzburg I.V., Ross M., Seifert F.A., Zussman J., Aoki K. & Gottardi G. 1988: Nomenclature of pyroxenes. 73, 1123–1133. https://doi.org/10.1180/minmag.1988.052.367.15

Palin R.M., Searle M.P., Waters D.J., Horstwood M.S.A. & Parrish R.R. 2012: Combined thermobarometry and geochronology of peraluminous metapelites from the Karakoram metamorphic complex, North Pakistan: New insight into the tectonothermal evolution of the Baltoro and Hunza Valley regions. *Journal of Metamorphic Geology* 30, 793–820. https://doi.org/10.1111/j.1525-1314.2012.00999.x

Palin R.M., Weller O.M., Waters D.J. & Dyck B. 2016: Quantifying geological uncertainty in metamorphic phase equilibria modelling; a Monte Carlo assessment and implications for tectonic interpretations. *Geoscience Frontiers* 7, 591–607. https://doi.org/10.1016/j.gsf.2015.08.005

Passchier C.W. & Trouw R.A.J. 2005: *Microtectonics*. 2nd Edition, Springer.

Phillips R.J., Searle M.P. & Parrish R.R. 2013: The geochemical and temporal evolution of the continental lithosphere and its relationship to continental-scale faulting: The Karakoram Fault, eastern Karakoram, NW Himalayas. *Geochemistry. Geophysics, Geosystems* 14, 583–603. https://doi.org/10.1002/ggge.20061

Powell R. & Holland T.J.B. 2008: On thermobarometry. *Journal of Metamorphic Geology* 26, 155–179. https://doi.org/10.1111/j.1525-1314.2007.00756.x

Putiš M., Nemec O., Ustalić S., Balen D., Sláma J., Babajić E., Soták J., Ružička P., Kurylo S. & Katanić P. 2025: Neotethyan Jurassic supra-subduction ophiolitic complex with Triassic subducted sole: Mineral chemistry, sole P–T estimates, and U/Pb geochronology of an intra-oceanic domain (Central Dinarides, Bosnia and Herzegovina). *Geochemistry* 85, 126263. https://doi.org/10.1016/j.chemer.2025.126263

Rolfo F., Lombardo B., Compagnoni R., Le Fort P., Lemennicier Y. & Pêcher A. 1997: Geology and Metamorphism of the Ladakh Terrane and Shyok Suture Zone in the Chogo Lungma – Turmik area (northern Pakistan). *Geodinamica Acta* 10, 251–270. https://doi.org/10.1080/09853111.1997.11105305

Rolland Y., Mahéo G., Guillot S. & Pêcher A. 2001: Tectono–metamorphic evolution of the Karakoram Metamorphic Complex (Dassu–Askole area, NE Pakistan): exhumation of mid–crustal HT–MP gneisses in a convergent context. *Journal of Metamorphic Geology* 19, 717–737. https://doi.org/10.1046/j.0263-4929.2001.00342.x

Rolland Y., Carrio-Schaffhauser E., Sheppard S.M.F., Pêcher A. & Esclauze L. 2006: Metamorphic zoning and geodynamic evolution of an inverted crustal section (Karakorum margin, N Pakistan), evidence for two metamorphic events. *International Journal of Earth Sciences* 95, 288–305. https://doi.org/10.1007/s00531-005-0026-x

Sanislav I.V. & Bell T.H. 2011: The inter-relationships between long-lived metamorphism, pluton emplacement and changes in the direction of bulk shortening during orogenesis. *Journal of Metamorphic Geology* 29, 513–536. https://doi.org/10.1111/j.1525-1314.2011.00928.x

Sapkota J. & Sanislav I.V. 2013: Preservation of deep Himalayan PT conditions that formed during multiple events in garnet cores: Mylonitization produces erroneous results for rims. *Tectonophysics* 587, 89–106. https://doi.org/10.1016/j.tecto.2012.10.029

Sayab M., Aerden D., Kuva J. & Hassan W.U. 2021: Tectonic evolution of the Karakoram metamorphic complex (NW Himalayas) reflected in the 3D structures of spiral garnets: Insights from X-ray computed micro-tomography. *Geoscience Frontiers* 12, 101113. https://doi.org/10.1016/j.gsf.2020.11.010

Searle M.P. & Hacker B.R. 2019: Structural and metamorphic evolution of the Karakoram and Pamir following India–Kohistan–Asia collision. *Geological Society, London, Special Publications* 483, 555–582. https://doi.org/10.1144/SP483.6

Searle M.P., Parrish R.R., Tirrul R. & Rex D.C. 1990: Age of crystallization and cooling of the K2 gneiss in the Baltoro Karakoram. *Journal of the Geological Society* 147, 603–606. https://doi.org/10.1144/gsjgs.147.4.0603

Searle M.P., Waters D.J., Dransfield M.W., Stephenson B.J., Walker C.B., Walker J.D. & Rex D.C. 1999: Thermal and mechanical models for the structural and metamorphic evolution of the Zanskar High Himalaya. *Geological Society, London, Special Publications* 164, 139–156. https://doi.org/10.1144/GSL.SP.1999.164.01.08

Searle M.P., Simpson R.L., Law R.D., Parrish R.R. & Waters D.J. 2003: The Structural Geometry, Metamorphic and Magmatic Evolution of the Everest Massif, High Himalaya of Nepal – South Tibet. *Journal of the Geological Society* 160, 345–366. https://doi.org/10.1144/0016-764902-126

Searle M.P., Parrish R.R., Thow A.V., Noble S.R., Phillips R.J. & Waters D.J. 2010: Anatomy, age and evolution of a collisional mountain belt: the Baltoro granite batholith and Karakoram Metamorphic Complex, Pakistani Karakoram. *Journal of the Geological Society* 167, 183–202. https://doi.org/10.1144/0016-76492009-043

Shah S.Z., Sayab M., Aerden D. & Khan M.A. 2011: Foliation intersection axes preserved in garnet porphyroblasts from the Swat area, NW Himalaya: A record of successive crustal shortening directions between the Indian plate and Kohistan–Ladakh Island Arc. *Tectonophysics* 509, 14–32. https://doi.org/10.1016/j.tecto.2011.05.010

Sharib A.S.A.A. & Bell T.H. 2011: Radical changes in bulk shortening directions during orogenesis: Significance for progressive development of regional folds and thrusts. *Precambrian Research* 188, 1–20. https://doi.org/10.1016/j.precamres.2011.03.008

Stübner K., Grujic D., Parrish R.R., Roberts N.M., Kronz A., Wooden J. & Ahmad T. 2014: Monazite geochronology unravels the timing of crustal thickening in NW Himalaya. *Lithos* 210, 111–128. https://doi.org/10.1016/j.lithos.2014.09.024

Tischendorf G., Förster H.-J., Ottesmann B. & Rieder M. 2007: True and brittle micas: Composition and solid-solution series. *Mineralogical Magazine* 71, 285–320. https://doi.org/10.1180/minmag.2007.071.3.285

Villa I., Ruffini R., Rolfo F. & Lombardo B. 1996: Diachronous metamorphism of the Ladakh Terrain at the Karakorum–Nanga Parbat–Haramosh junction (NW Baltistan, Pakistan). *Schweizerische Mineralogische und Petrographische Mitteilungen* 76, 245–264. https://doi.org/10.7892/boris.87207

Weller O.M., St-Onge M.R., Waters D.J., Rayne N., Searle M.P., Chung S.-L., Palin R.M., Lee Y.-H. & Xu X. 2013: Quantifying Barrovian metamorphism in the Danba structural culmination of eastern Tibet. *Journal of Metamorphic Geology* 31, 909–935. https://doi.org/10.1111/jmg.12050

White R.W., Powell R. & Holland T.J.B. 2007: Progress relating to calculation of partial melting equilibria for metapelites. *Journal of Metamorphic Geology* 25, 511–527. https://doi.org/10.1111/j.1525-1314.2007.00711.x

White R.W., Powell R., Holland T.J.B., Johnson T.E. & Green E.C.R. 2014: New mineral activity–composition relations for thermodynamic calculations in metapelitic systems *Journal of Metamorphic Geology* 31, 261–286. https://doi.org/10.1111/jmg.12071

Woodsworth G.J. 1977: Homogenisation of zoned garnets from pelitic schists. *The Canadian Mineralogist* 15, 230–242.

Xiang H. & Connolly J.A. 2022: GeoPS: An interactive visual computing tool for thermodynamic modelling of phase equilibria. *Journal of Metamorphic Geology* 40, 243–255. https://doi.org/10.1111/jmg.12626

Zhu D.-C., Zhao Z.-D., Niu Y., Dilek Y., Hou Z.-Q. & Mo X.-X. 2013: The origin and pre-Cenozoic evolution of the Tibetan Plateau. *Gondwana Research* 23, 1429–1454. https://doi.org/10.1016/j.gr.2012.02.002

Zubovich A., Schone T., Metzger S., Mosienko O., Mukhamediev S., Shahshebaev A. & Zach C. 2016: Tectonic interaction between the Pamir and Tien Shan observed by GPS. *Tectonics* 35, 283–292. https://doi.org/10.1002/2015TC004055